
This is an electronic reprint of the original article.

This reprint may differ from the original in pagination and typographic detail.

Saikia, Payaswini; Russell, David M.; Baglio, M. C.; Bramich, D. M.; Casella, Piergiorgio; Trigo, Maria Diaz; Gandhi, Poshak; Jiang, Jiachen; Maccarone, Thomas; Soria, Roberto; Al Noori, Hind; Al Yazeedi, Aisha; Alabarta, Kevin; Belloni, Tomaso; Bel, Marion Cadolle; Ceccobello, Chiara; Corbel, Stéphane; Fender, Rob; Gallo, Elena; Homan, Jeroen; Koljonen, Karri; Lewis, Fraser; Markoff, Sera B.; Miller-Jones, James C.A.; Rodriguez, Jerome; Russell, Thomas D.; Shahbaz, Tariq; Sivakoff, Gregory R.; Testa, Vincenzo; Tetarenko, Alexandra J.

A Multiwavelength Study of GRS 1716-249 in Outburst

Published in:

The Astrophysical Journal

DOI:

[10.3847/1538-4357/ac6ce1](https://doi.org/10.3847/1538-4357/ac6ce1)

Published: 01/06/2022

Document Version

Publisher's PDF, also known as Version of record

Published under the following license:

CC BY

Please cite the original version:

Saikia, P., Russell, D. M., Baglio, M. C., Bramich, D. M., Casella, P., Trigo, M. D., Gandhi, P., Jiang, J., Maccarone, T., Soria, R., Al Noori, H., Al Yazeedi, A., Alabarta, K., Belloni, T., Bel, M. C., Ceccobello, C., Corbel, S., Fender, R., Gallo, E., ... Tetarenko, A. J. (2022). A Multiwavelength Study of GRS 1716-249 in Outburst: Constraints on Its System Parameters. *The Astrophysical Journal*, 932(1), Article 38. <https://doi.org/10.3847/1538-4357/ac6ce1>

This material is protected by copyright and other intellectual property rights, and duplication or sale of all or part of any of the repository collections is not permitted, except that material may be duplicated by you for your research use or educational purposes in electronic or print form. You must obtain permission for any other use. Electronic or print copies may not be offered, whether for sale or otherwise to anyone who is not an authorised user.



A Multiwavelength Study of GRS 1716-249 in Outburst: Constraints on Its System Parameters

Payaswini Saikia^{1,2}, David M. Russell^{1,2}, M. C. Baglio^{1,2,3}, D. M. Bramich^{1,4}, Piergiorgio Casella⁵, Maria Diaz Trigo⁶, Poshak Gandhi⁷, Jiachen Jiang⁸, Thomas Maccarone⁹, Roberto Soria^{10,11}, Hind Al Noori¹², Aisha Al Yazeedi^{1,2}, Kevin Alabarta^{1,2,13,14}, Tomaso Belloni³, Marion Cadolle Bel¹⁵, Chiara Ceccobello¹⁶, Stéphane Corbel^{17,18}, Rob Fender^{19,20}, Elena Gallo²¹, Jeroen Homan²², Karri Koljonen^{23,24,25}, Fraser Lewis^{26,27}, Sera B. Markoff^{28,29}, James C. A. Miller-Jones³⁰, Jerome Rodriguez¹⁷, Thomas D. Russell³¹, Tariq Shahbaz^{32,33}, Gregory R. Sivakoff³⁴, Vincenzo Testa⁵, and Alexandra J. Tetarenko^{9,35}

¹ Center for Astro, Particle and Planetary Physics, New York University Abu Dhabi, PO Box 129188, Abu Dhabi, United Arab Emirates; ps164@nyu.edu

² New York University Abu Dhabi, PO Box 129188, Abu Dhabi, United Arab Emirates

³ INAF, Osservatorio Astronomico di Brera, Via E. Bianchi 46, I-23807 Merate (LC), Italy

⁴ Division of Engineering, New York University Abu Dhabi, PO Box 129188, Abu Dhabi, United Arab Emirates

⁵ INAF, Osservatorio Astronomico di Roma Via Frascati 33—Monte Porzio Catone, Italy

⁶ ESO, Karl-Schwarzschild-Strasse 2, D-85748 Garching bei München, Germany

⁷ School of Physics & Astronomy, University of Southampton, Highfield, Southampton SO17 1BJ, UK

⁸ Institute of Astronomy, University of Cambridge, Madingley Road, Cambridge CB3 0HA, UK

⁹ Department of Physics & Astronomy, Texas Tech University, Box 41051, Lubbock TX 79409-1051, USA

¹⁰ College of Astronomy and Space Sciences, University of the Chinese Academy of Sciences, Beijing 100049, People's Republic of China

¹¹ Sydney Institute for Astronomy, School of Physics A28, The University of Sydney, Sydney, NSW 2006, Australia

¹² Department of Physics, University of California, Santa Barbara, CA 93106, USA

¹³ Kapteyn Astronomical Institute, University of Groningen, PO Box 800, NL-9700 AV Groningen, The Netherlands

¹⁴ School of Physics and Astronomy, University of Southampton, Southampton, SO17 1BJ, UK

¹⁵ Allane SE, Dr.-Carl-von-Linde-Str. 2, D-82049 Pullach, Munich, Germany

¹⁶ Department of Space, Earth and Environment, Chalmers University of Technology, Onsala Space Observatory, SE-439 92 Onsala, Sweden

¹⁷ AIM, CEA, CNRS, Université de Paris, Université Paris-Saclay, F-91191 Gif-sur-Yvette, France

¹⁸ Station de Radioastronomie de Nan'ay, Observatoire de Paris, PSL Research University, CNRS, Univ. Orléans, F-18330 Nançay, France

¹⁹ Department of Physics, University of Oxford, Denys Wilkinson Building, Keble Road, Oxford OX1 3RH, UK

²⁰ Department of Astronomy, University of Cape Town, Private Bag X3, Rondebosch 7701, South Africa

²¹ Department of Astronomy, University of Michigan, 1085 S University, Ann Arbor, Michigan 48109, USA

²² Eureka Scientific, Inc., Oakland, CA 94602, USA

²³ Finnish Centre for Astronomy with ESO (FINCA), Vesilinnantie 5, FI-20014 University of Turku, Finland

²⁴ Institutt for Fysikk, Norwegian University of Science and Technology, Trondheim, Norway

²⁵ Aalto University Metsähovi Radio Observatory, Metsähovintie 114, 02540 Kylmala, Finland

²⁶ Faulkes Telescope Project, School of Physics and Astronomy, Cardiff University, The Parade, Cardiff, CF24 3AA, Wales, UK

²⁷ Astrophysics Research Institute, Liverpool John Moores University, 146 Brownlow Hill, Liverpool L3 5RF, UK

²⁸ Anton Pannekoek Institute for Astronomy, University of Amsterdam, Science Park 904, 1098 XH Amsterdam, The Netherlands

²⁹ Gravitation & AstroParticle Physics Amsterdam (GRAPPA), University of Amsterdam, Science Park 904, 1098 XH Amsterdam, The Netherlands

³⁰ International Centre for Radio Astronomy Research, Curtin University, GPO Box U1987, Perth, WA 6845, Australia

³¹ INAF, Istituto di Astrofisica Spaziale e Fisica Cosmica, Via U. La Malfa 153, I-90146 Palermo, Italy

³² Instituto de Astrofísica de Canarias (IAC), E-38205 La Laguna, Tenerife, Spain

³³ Departamento de Astrofísica, Universidad de La Laguna (ULL), E-38206 La Laguna, Tenerife, Spain

³⁴ Department of Physics, University of Alberta, CCIS 4-181, Edmonton, AB, T6G 2E1, Canada

Received 2022 March 14; revised 2022 April 28; accepted 2022 May 3; published 2022 June 14

Abstract

We present a detailed study of the evolution of the Galactic black hole transient GRS 1716–249 during its 2016–2017 outburst at optical (Las Cumbres Observatory), mid-infrared (Very Large Telescope), near-infrared (Rapid Eye Mount telescope), and ultraviolet (the Neil Gehrels Swift Observatory Ultraviolet/Optical Telescope) wavelengths, along with archival radio and X-ray data. We show that the optical/near-infrared and UV emission of the source mainly originates from a multi-temperature accretion disk, while the mid-infrared and radio emission are dominated by synchrotron emission from a compact jet. The optical/UV flux density is correlated with the X-ray emission when the source is in the hard state, consistent with an X-ray irradiated accretion disk with an additional contribution from the viscous disk during the outburst fade. We find evidence for a weak, but highly variable jet component at mid-infrared wavelengths. We also report the long-term optical light curve of the source and find that the quiescent i' -band magnitude is 21.39 ± 0.15 mag. Furthermore, we discuss how previous estimates of the system parameters of the source are based on various incorrect assumptions, and so are likely to be inaccurate. By comparing our GRS 1716–249 data set to those of other outbursting black hole X-ray binaries, we find that while GRS 1716–249 shows similar X-ray behavior, it is noticeably optically fainter, if the literature distance of 2.4 kpc

is adopted. Using several lines of reasoning, we argue that the source distance is further than previously assumed in the literature, likely within 4–17 kpc, with a most likely range of ~ 4 –8 kpc.

³⁵ NASA Einstein Fellow.



Unified Astronomy Thesaurus concepts: Astrophysical black holes (98); Accretion (14); Jets (870); X-ray binary stars (1811); Low-mass x-ray binary stars (939); Black hole physics (159)

Supporting material: machine-readable tables

1. Introduction

Black hole X-ray binaries (BHXBs) are interacting binary systems composed of a black hole (BH) accreting matter from a secondary companion star. The accreted matter forms a differentially rotating disk around the BH known as an accretion disk (Shakura & Sunyaev 1973). A large fraction of the accretion energy is often channeled into relativistic, collimated outflows known as jets (e.g., Blandford & Konigl 1979; Fender et al. 2004). Many BHXBs are transient in nature, alternating between periods of quiescence (typically lasting years to decades, with the X-ray luminosities in the range of 10^{30-33} erg s⁻¹) and outburst (typically lasting weeks to months, with X-ray luminosities reaching 10^{36-39} erg s⁻¹, e.g., Corral-Santana & Casares 2016; Tetarenko et al. 2016).

During an outburst, many BHXBs undergo hysteresis in the spectral state transitions following a q-shaped evolutionary pattern in the hardness-intensity diagram (HID; Miyamoto et al. 1995; Homan et al. 2001; Homan & Belloni 2005; Belloni 2010). The rise of the outburst is generally dominated by a hard, power-law-like spectral component (with photon index $\Gamma < 2$) with a high-energy cutoff at 50–100 keV. This is known as the hard state (HS), which is usually associated with thermal Comptonization due to Compton up-scattering of soft disk photons by a corona of hot electrons (e.g., Thorne & Price 1975; Sunyaev & Titarchuk 1980; Done et al. 2007). During the HS, collimated compact jets are launched, emitting self-absorbed synchrotron emission that dominates radio through infrared (IR) wavelengths (e.g., Corbel et al. 2000; Fender et al. 2004), in analogy with those observed in active galactic nuclei (Blandford & Konigl 1979; Hjellming & Johnston 1988). Many BHXBs in the HS follow a nonlinear radio/X-ray luminosity correlation, where $L_R \propto L_X^\beta$ with $\beta \sim 0.5-0.7$ (e.g., Corbel et al. 2003, 2013; Gallo et al. 2018), which extends to active galactic nuclei through the fundamental plane of BH activity (Merloni et al. 2003; Falcke et al. 2004; Saikia et al. 2015, 2018), suggesting scale invariance of compact jets.

During the peak and decay of an outburst, when the system is said to be in the soft state (SS), the spectra are dominated by a soft, blackbody-like spectral component due to an optically thick, geometrically thin accretion disk (Shakura & Sunyaev 1973). The jets are suppressed in this state (e.g., Tananbaum et al. 1972; Fender et al. 1999; Coriat et al. 2011; Russell et al. 2011; Koljonen et al. 2018; Russell et al. 2019; Carotenuto et al. 2021). During the transition between these two states, the system enters the intermediate state (IS), dominated by a thermal disk component with a color temperature of 0.1–1 keV, which is further classified based on the X-ray timing properties into hard-intermediate and soft-intermediate states (e.g., Homan & Belloni 2005; Belloni 2010). Depending on the source state, fast variability can be observed, including quasi-periodic oscillations (QPOs), that have been classified into three types: A, B, and C (e.g., Ingram & Motta 2019). A number of BHXBs remain in the HS for the entire duration of the outburst (or only transition to the hard-intermediate state). These are referred to as “hard-only state outbursts” (Tetarenko et al. 2016), “low/hard state outbursts”

(Belloni et al. 2002), “failed outbursts” (e.g., Capitanio et al. 2009; Curran & Chaty 2013), “failed state transition outbursts” (Bassi et al. 2019), or “failed-transition outbursts” (Alabarta et al. 2021).

1.1. GRS 1716–249

In 1994 September, GRS 1716–249 had a series of several X-ray re-flares or mini-outbursts, as observed by both SIGMA and BATSE at the level of $\sim 10\%$ of its peak value in 1993 (Revnivtsev et al. 1998). During this period, the X-ray light curve was dominated by at least four sawtooth-like re-brightening events with slow rise ($\sim 30-70$ days) and dramatic decay (~ 10 days), accompanied by simultaneous radio flares following the onset of decays (Hjellming et al. 1996). This re-brightening event lasted ~ 400 days and had at least four separate peaks in hard X-rays.

The source had another outburst after almost 21 yr in quiescence, and was detected by the Monitor of All-sky X-ray Image (MAXI) on 2016 December 18 (MJD 57740, Negoro et al. 2016), with a photon index of $\Gamma = 1.62 \pm 0.06$ on 2016 December 21 (MJD 57743, Masumitsu et al. 2016). It was found to be in the hard spectral state with Chandra X-ray Observatory observations on 2017 February 6 (MJD 57790, Miller et al. 2017) and International Gamma-Ray Astrophysics Laboratory (INTEGRAL) observations on 2017 February 10 (MJD 57794, Del Santo et al. 2017). The source was then seen transitioning to the hard-intermediate state for some time with Neil Gehrels Swift Observatory (Swift) observations on 2017 March 27 and April 2 (MJD 57839 and MJD 57845, Armas Padilla & Munoz-Darias 2017), and then returning to the hard state after a failed-transition outburst to the soft state on 2017 May 5 and 11 (MJD 57878 and MJD 57884, Bassi et al. 2017), as was also the case in the 1993 event (Revnivtsev et al. 1998). Bassi et al. (2019) studied the HID of the source and found that it had three softening events when the source transitioned from the hard to the hard-intermediate state. Along with the three softest points (MJD 57854.2, 57895.9 and 57960.7), we consider all the dates with hardness ratio $\lesssim 0.7$, which lies in the range of 2017 July 6 and August 13 (MJD 57940–57978) as the hard-intermediate state. The source was found to be one of the “outlier” BHXBs (Bassi et al. 2019) in the radio/X-ray correlation plane (which are radio fainter by 1–2 orders of magnitude, and tend to have a steeper correlation index, with $\beta \sim 1.4$, e.g., Corbel et al. 2004; Coriat et al. 2011; Gallo et al. 2012). A type-C quasi-periodic oscillation (QPO) was also detected in the hard state (Bharali et al. 2019), and signatures of a hot and dense accretion disk wind (with terminal velocity ~ 2000 km s⁻¹) were observed (Cuneo et al. 2020). From the broadband spectral fitting of the source, the irradiated accretion disk was found to dominate the optical emission, while a hint of an excess near-IR emission above the prediction of the irradiated disk model was observed, likely due to synchrotron emission originated in the jet (Rout et al. 2021).

1.2. System Parameters of GRS 1716–249

The system parameters of GRS 1716–249 are not well constrained. From the 1993 outburst, della Valle et al. (1994) proposed that the system contains a low-mass main-sequence star with spectral type K (or later), at a possible distance between 2.2 kpc (lower limit obtained from the equivalent width of the NaD absorption lines) and 2.8 kpc (upper limit based on an incorrect maximum luminosity of an X-ray transient). But in light of several arguments we explore in Section 4.2.2., we find that the estimated upper limit of 2.8 kpc is not a reliable constraint for its distance. Masetti et al. (1996) discovered super humps in the light curve (although these could also be due to irradiation modulation, see Section 4.2.1 for a discussion). Assuming that the donor is a main-sequence star, they estimated the companion star mass to be $\sim 1.6 M_{\odot}$ and inferred an orbital period of ~ 0.6127 days or ~ 14.7 hr for a Roche lobe-filling star. Then they used the maximum mass ratio criterion for having super humps, which is about 3:1, and proposed that the mass of the accreting compact object is $> 4.9 M_{\odot}$, hence classifying it as a black hole. They also suggested that a $1.6 M_{\odot}$ main-sequence star at 2.4 ± 0.4 kpc would exceed the quiescent luminosity of the binary substantially (although it is important to note that the quiescent luminosity limit of the source was not confidently known, see Section 3.6). Despite all the crude assumptions employed, these limits on the mass of the compact object and the distance to the source have been used for all subsequent studies on the source, until this paper.

During the 2016–2017 outburst, GRS 1716–249 was extensively studied in the X-ray wavelengths. Tao et al. (2019) used spectral fits of three NuSTAR and Swift data sets in its hard-intermediate state, and constrained the black hole mass to be $< 8 M_{\odot}$ at a 90% confidence level under the assumption that the distance to the source is 2.4 ± 0.4 kpc. Using the same assumption, they also inferred the inclination angle of the inner disk to be in the range of 40° – 50° by performing joint modeling of the continuum and the reflection components. An analysis of the broadband (1–78 keV) X-ray spectra of the source taken by NuSTAR and Swift constrained the accretion disk density parameter of GRS 1716–249 to be in the range of 10^{19} – 10^{20} cm^{-3} (Jiang et al. 2020). Recently, the black hole mass was claimed to lie in the range of 4.5 – $5.9 M_{\odot}$ according to a two-component advective flow (TCAF) model (Chatterjee et al. 2021), although this method uses model-dependent spectral fitting of the source to obtain these values.

In this paper, we present a detailed multiwavelength study of GRS 1716–249 during its 2016–2017 outburst, with particular focus on its UV/optical/IR emission to investigate the physical mechanisms contributing to the emission in these wave bands, and reveal the system parameters of the source. In Section 2, we describe in detail the observations and the analyses of the data used for this study. In Section 3, we present the characteristics of the outburst using various tools like the light curves, variability of the source during the peak of the outburst using fractional rms values, the optical/UV spectra of the source, the broadband spectral energy distributions (SEDs), the color–magnitude diagrams to study the color evolution of the source during the outburst, and the optical/UV/X-ray correlations to explore the various emission mechanisms. We also report long-term (~ 10 yr) monitoring of the source and discuss its quiescent optical magnitude, which is important as the optical brightness of BHXBs in quiescence has minimal

contribution from the accretion disk and is dominated by the companion star (Chevalier et al. 1989). In Section 4, we interpret and discuss our results, including the implications of our analyses on the system parameters of the source, and present new estimates for the distance to the source. Finally, we present our conclusions in Section 5.

2. Observations and Data Reduction

2.1. Optical Observations

2.1.1. LCO Optical Data

We monitored GRS 1716–249 during its 2016–2017 outburst extensively with the Las Cumbres Observatory (LCO) between 2017 January 28 and October 21 (MJD 57781–58046). Observations were made using the 1 m LCO telescopes at Siding Spring Observatory, Australia, Cerro Tololo Inter-American Observatory, Chile, and the South African Astronomical Observatory (SAAO), South Africa, as well as the 2 m Faulkes Telescopes at Haleakala Observatory, Maui, Hawai‘i, USA and Siding Spring Observatory, Australia. The source was also monitored during quiescence, before and after the 2016–2017 outburst, for 11 yr since 2006 February, as part of an ongoing monitoring campaign of ~ 50 low-mass X-ray binaries (LMXB) coordinated by the Faulkes Telescope Project (Lewis et al. 2008; Lewis 2018).

Imaging data were primarily taken in the Sloan Digital Sky Survey (SDSS) g' , r' , i' , and the Panoramic Survey Telescope and Rapid Response System (Pan-STARRS) Y -band filters, with some data also taken in Bessel B and V bands. The data were initially processed using the LCO BANZAI pipeline (McCully et al. 2018). The multi-aperture photometry on the reduced data was performed using “X-ray Binary New Early Warning System (XB-NEWS)”, a real-time data analysis pipeline that aims to detect and announce new X-ray binary outbursts within a day of the first optical detection of an outburst (e.g., Russell et al. 2019; Goodwin et al. 2020; Pirbhoy et al. 2020). The XB-NEWS pipeline downloads new images of all targets of interest from the LCO archive along with their associated calibration data and performs several quality control steps to ensure that only good quality images are analyzed. XB-NEWS then computes an astrometric solution for each image using Gaia DR2 positions,³⁶ performs aperture photometry of all the stars in the image, solves for zero-point calibrations between epochs (Bramich & Freudling 2012), and flux calibrates the photometry using the ATLAS All-Sky Stellar Reference Catalog (ATLAS-REFCAT2, Tonry et al. 2018). The pipeline also performs multi-aperture photometry (azimuthally averaged PSF profile fitting photometry, Stetson 1990). Light curves are produced in near real-time. If the location of the source is well-known, but the source is fainter than the formal detection threshold, the pipeline performs forced photometry on the position. Magnitude errors larger than ~ 0.25 mag are considered as marginal detections and are not included in our study.

We detected the source during outburst in a total of 192 images between 2017 January 28 (MJD 57781) and 2017 October 21 (MJD 58046), generally at a cadence of every 2–3 days during the brighter phase of the outburst, and every ~ 75 s for the high cadence images taken on 2017 May 9 (MJD 57882). A detailed observation log containing information

³⁶ <https://www.cosmos.esa.int/web/gaia/dr2>

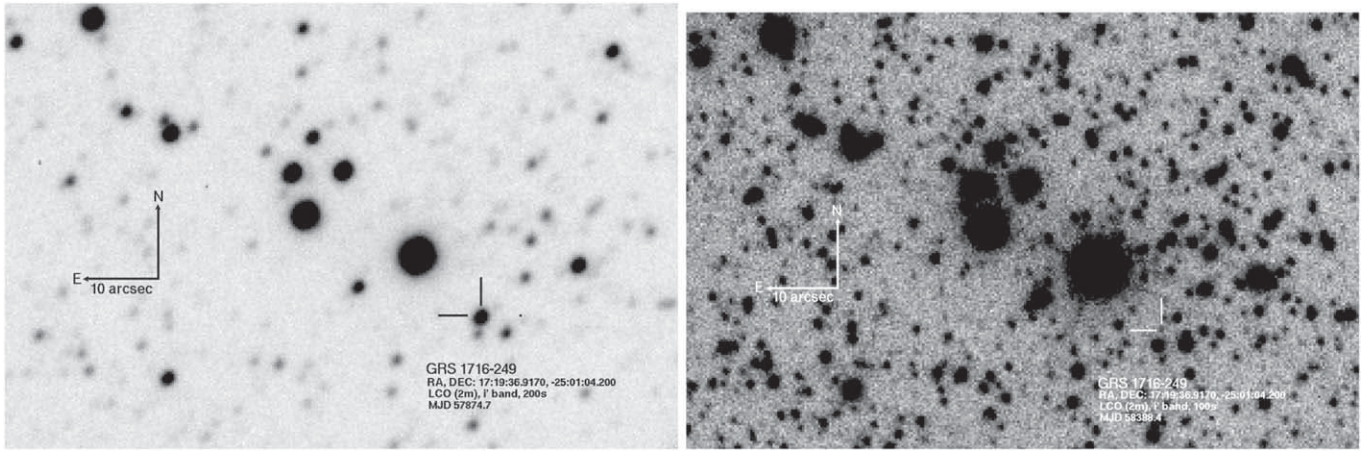


Figure 1. The left panel shows the optical finding chart of GRS 1716–249 during outburst (MJD 57874.7) with the 2 m LCO telescope in the i' -band with 200 s exposure time. Previously, a lower-resolution optical finding chart during outburst is available in the V band (Masetti et al. 1996). The target is indicated with hash mark in both the panels. The right panel shows the quiescent optical finding chart (MJD 58388.4) with the 2 m LCO telescope in the i' band with 100 s exposure time (an image taken under excellent conditions, with seeing of $0''.82$). The counterpart is just $1''.6$ from a star of similar magnitude to the north of GRS 1716-249.

about the LCO epochs, filters and magnitudes, is summarized in the Appendix. From our XB-NEWS optical analysis, the accurate optical position of the source was found to be R.A.: $17:19:36.917$ and decl.: $-25:01:04.20$ (J2000), consistent with the VLBI coordinates to within $\lesssim 0''.1$ (Atri et al. 2019). The optical finding charts in the i' band during both outburst and quiescence, are shown in Figure 1. The systematic error in the position measurement is small ($\lesssim 0''.3$) and has better precision than previously reported optical measurements ($\sim 1''$ in della Valle et al. 1994). To convert the multi-aperture photometry magnitudes obtained from the XB-NEWS pipeline to the intrinsic de-reddened flux densities, we use the absorption column density $N_H = (0.70 \pm 0.01) \times 10^{22} \text{ cm}^{-2}$, as reported in Bassi et al. (2020). Using the relation between optical extinction and hydrogen column density (Foight et al. 2016), the V -band absorption coefficient is inferred as $A_V = 2.44 \pm 0.11 \text{ mag}$. There are different determinations of the relation between extinction and hydrogen column density in the literature (see, e.g., Guver & Ozel 2009; Watson 2011; Willingale et al. 2013), but we use the Foight et al. (2016) value as they provide the most recent estimates using updated abundances and hence are likely more reliable. We note that Bahramian et al. (2015) also arrive at a similar relation using the updated abundances, while including X-ray binaries in their sample. This leads to a color excess of $E(B - V) \sim 0.8 \text{ mag}$ (assuming a mean value of $A_V/E(B - V) \sim 3.1$ for the diffuse interstellar medium, Fitzpatrick 1999), which is consistent with the historical value of $E(B - V) \sim 0.9 \pm 0.2 \text{ mag}$ (della Valle et al. 1994) obtained based on multiple lines of reasoning. The wavelength-dependent extinction terms, used for de-reddening in other bands, are obtained from the extinction curve of Cardelli et al. (1989).

2.1.2. Archival Optical Data

We also use the archival data of the source obtained in the G spectral filter with the Gaia telescope³⁷ during the recent outburst. Gaia first detected the source on 2017 January 27 (MJD 57780.8) at $G = 16.44$. Prior to that, the last observation it had on 29 October 2016 (MJD 57690) was a non-detection

(typical detection limit of Gaia is $\sim 20.7 \text{ mags}$, Brown et al. 2016). Gaia detected GRS 1716–249 on 13 days during the outburst, with the last detection on 2017 September 23 (MJD 58019). We use these public data in Figure 2, while studying the optical light curve of the source.

2.1.3. Archival Historical Optical Data

To compare the 2016–2017 outburst of the source with its discovery outburst from 1993, we include the simultaneous optical detections taken on 1993 October 8 (MJD 49268) in the B , V , and R filters as 17.7 ± 0.1 , 16.7 ± 0.1 , and $16.0 \pm 0.1 \text{ mags}$, respectively (della Valle et al. 1994). We also use the historical B - and V -band observations from Masetti et al. (1996). We use these data in the spectral energy distribution study (see Section 3.3) and the detailed analysis of the evolution of the source through the color–magnitude diagram (see Section 3.5).

2.2. Infrared Observations

2.2.1. VISIR Mid-IR Observations

We acquired targeted observations of GRS 1716–249 with the Very Large Telescope (VLT) in mid-IR wavelengths on three nights during the 2016–2017 outburst, using the VLT Imager and Spectrometer for the mid-IR (VISIR; Lagage et al. 2004) instrument on the VLT’s UT3 (Melipal). The observations were made under the programs 098.D-0893 and 099.D-0884 (PI : D. Russell) in the M band ($4.15\text{--}5.19 \mu\text{m}$), $J8.9$ ($8.00\text{--}9.43 \mu\text{m}$), $B10.7$ ($9.28\text{--}12.02 \mu\text{m}$), and PAH2 _2 ($11.5\text{--}12.3 \mu\text{m}$) filters on 2017 March 25 (MJD 57837), April 21 (MJD 57864), and April 22 (MJD 57865), for approximately 40–45 minutes total telescope time on each date. The integration time on source was usually 25 minutes, with additional substantial overheads due to the chopping and nodding pattern. The observing conditions were photometric during the observations of GRS 1716–249 on March 25 and April 22, and were clear with some humidity on April 21. Nevertheless, standard stars taken just before and after GRS 1716–249 were used to achieve accurate flux calibration on April 21. The detailed VISIR observing log and the photometric results are reported in Table 1.

³⁷ <http://gsaweb.ast.cam.ac.uk/alerts/alert/Gaia17agz/>

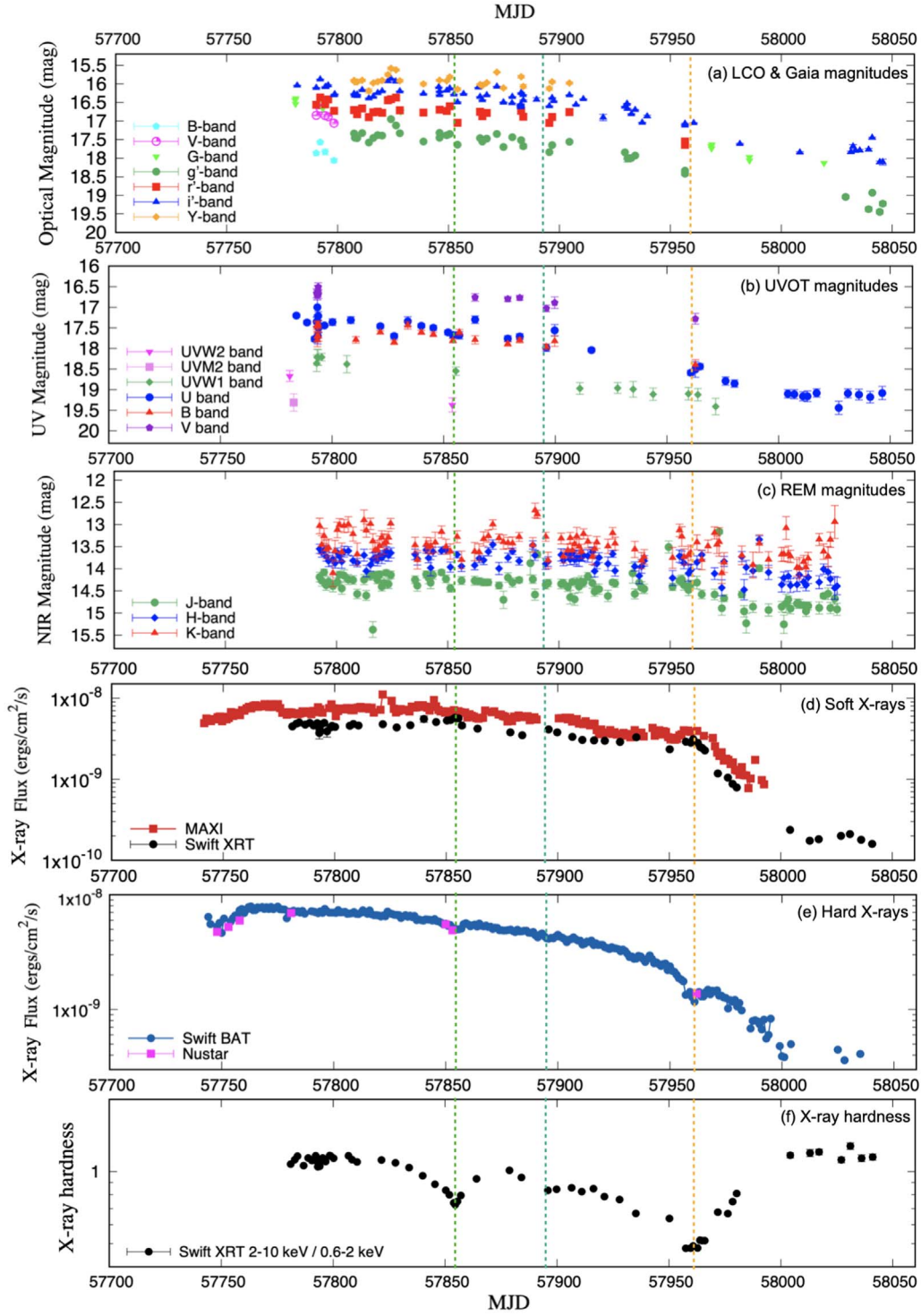


Figure 2. Light curves of the 2016–2017 outburst of GRS 1716–249 in different wavelengths. The three vertical dashed lines depict the softest points in each of the three softening events when the source transitioned from the hard to the hard-intermediate state, as reported by Bassi et al. (2019), on MJD 57854.2 (green), MJD 57895.9 (blue), and MJD 57960.7 (yellow). (a) The optical light curves from the LCO telescopes in *B*, *V*, *g'*, *r'*, *i'*, and *Y* bands, and from the Gaia telescope in *G* band. (b) The UV light curves represent Vega magnitudes from Swift UVOT in *UVW2*, *UVM2*, *UVM1*, *U*, *B*, and *V* filters. (c) The near-IR light curves with vega magnitudes obtained with the REM telescope; here we show the *J*, *H*, and *K* magnitudes of the source blended with a non-variable 2MASS star with magnitudes $J = 15.33 \pm 0.06$, $H = 14.46 \pm 0.06$, and $K = 14.16 \pm 0.08$ (see text). (d) The soft X-ray fluxes obtained from Swift/XRT in the 2–10 keV and MAXI/GSC in the 2–20 keV range, plotted in a logarithmic scale. (e) The hard X-ray fluxes obtained with Swift/BAT and NuSTAR in the 15–50 keV telescopes, plotted in a logarithmic scale. We only plot the 5σ detections in the X-rays, converting the source count rate to fluxes, assuming a photon index of $\Gamma = 1.68 \pm 0.01$ and $N_H = (0.70 \pm 0.01) \times 10^{22} \text{ cm}^{-2}$ (Bassi et al. 2020). (f) X-ray hardness from Swift/XRT showing the ratio of X-ray fluxes in the ranges of 2–10 keV and 0.6–2 keV.

The data were reduced using the VISIR pipeline in the *gasgano* environment. We combined the raw images from the chop/nod cycle and performed aperture photometry in IRAF

using a large enough aperture to minimize the effect of small seeing variations on the fraction of flux in the aperture (the method is the same as that used in Baglio et al. 2018). To flux

Table 1

Observation Log and Results of the Mid-IR Photometry Performed on GRS 1716–249 with the VISIR Instrument in 2017 March and April, Tabulating the Start of Observing Time, Filter Used and the Central Wavelength, Weather Condition, and Airmass at Mid-observation, the Exposure Time for Each Observation, Flux Density of the Detections and the 3σ Upper Limits for Non-detections, and a List of the Standard Stars Observed within a Month of Our Observation

Epoch (UT) Start Time (MJD)	Filter	Wavelength (μm)	Weather Conditions	Airmass	Exposure (s)	Flux Density (mJy)	Standard Stars Within a Month
2017.03.25 06:29:22 (57837)	<i>B10.7</i>	10.64	Photometric	1.398	1500	<1.35	1–9
2017.03.25 07:30:25 (57837)	<i>J8.9</i>	8.70	Photometric	1.165	1500	<1.37	10
2017.03.25 08:18:47 (57837)	<i>PAH2_2</i>	11.68	Photometric	1.066	1500	<3.16	10
2017.04.21 08:59:26 (57864)	<i>J8.9</i>	8.70	Clear, humid	1.029	1500	3.22 ± 0.59	11, 12
2017.04.22 08:24:43 (57865)	<i>PAH2_2</i>	11.68	Photometric	1.007	1200	<2.36	11,13–16
2017.04.22 09:03:19 (57865)	<i>M-band</i>	4.67	Photometric	1.035	1500	<2.71	11,15,16

Note. The reported fluxes are not de-reddened. Standard stars used are 1, HD039523; 2, HD046037; 3, HD047667; 4, HD061935; 5, HD075691; 6, HD097576; 7, HD099167; 8, HD111915; 9, HD133774; 10, HD145897; 11, HD151680; 12, HD178345; 13, HD082668; 14, HD108903; 15, HD123139; and 16, HD163376.

calibrate the photometry and estimate the flux density of the source, we used all the standard star observations taken within one month of the observation night in the same filter during clear sky conditions. All the standard stars used are listed in the final column of Table 1. At mid-IR wavelengths, the zero-point corrections rarely vary much. In fact, we found that the ADU/flux conversion factor measured from different standard star observations within a month varied only by 5%–10% when the airmass is less than 1.5. For all the filters for which we had only one standard star available within one month of the observation, we use an error of 5% in the ADU to calculate the uncertainty on the flux density of the source.

The source was only detected on one date, April 21, in the *J8.9* filter, with a magnitude of 18.24 ± 0.19 , or a flux density of 3.22 ± 0.59 mJy (the detection has a signal-to-noise ratio of 6.2). Although the photometric error for the detection is small, the uncertainty in the flux density is increased due to systematic errors arising from the limited number of available standard stars within a month of the detection. On the other two dates when the source was not detected, we derive 3σ upper limits from the root mean square (rms) in a region centered on the position of GRS 1716–249. The closest WISE catalog star is $12''$ away from the position of GRS 1716–249 (outside the field-of-view of VISIR), with a flux density of 2.24 mJy at $12 \mu\text{m}$.

2.2.2. REM Near-IR Observations

We observed GRS 1716–249 in the near-IR wavelengths (*J*, *H*, and *K* bands, one filter at a time) with the REMIR camera mounted on the Rapid Eye Mount (REM; La Silla, Chile) telescope between 2017 February 8 and October 1 (MJD 57792–58027). For each epoch, the reduction of the images was performed by subtracting the sky contribution; this was obtained as the median of five misaligned exposures of 60 s and 30 s in the *J* and *H* filter, respectively, and of 10×15 s exposures in the *K* band. Once the sky was subtracted, we registered and averaged the exposures to enhance the signal to noise.

We performed aperture photometry on each reduced image using IRAF. The magnitudes were then calibrated against a group of five 2MASS reference stars in the field. We note that a 2MASS star is observed at a distance of $\sim 3''5$ from the target in the REM images. Considering the spatial resolution of REMIR ($1''.22 \text{ pixel}^{-1}$) and the seeing, the two stars are therefore blended together in all images. Under the reasonable hypothesis that the 2MASS star is not variable, we subtract the

contribution of the 2MASS star from the flux extracted with our analysis to build spectral energy distributions. The magnitudes of the 2MASS star are tabulated in the 2MASS catalog ($J = 15.33 \pm 0.06$; $H = 14.46 \pm 0.06$; $K = 14.16 \pm 0.08$). To double check, we found and downloaded archival *J*-band images of the field taken with the SOFI instrument at the New Technology Telescope (NTT; La Silla, Chile) during quiescence in 1999 (July 5 and 7; Program ID: 63. H-0232). The *J*-band magnitude of the 2MASS star, after calibration, is $J = 15.38 \pm 0.05$, entirely consistent with the value reported in the 2MASS catalog (which suggests that source has probably been stable over the years). We tabulate the REM epochs, filters, and magnitudes in the Appendix (see Table A2).

2.2.3. Archival Near-IR Observations

We use the archival near-IR photometric observations of GRS 1716–249 during the outburst. Bassi et al. (2020) reported near-IR detections of the source obtained with the Rapid Eye Mount telescope (REM) on 2017 February 9 (MJD 57793) of $J = 14.18 \pm 0.22$, $H = 13.81 \pm 0.14$, and $K = 13.84 \pm 0.29$ and 13.59 ± 0.16 , with exposure times of 300 s, 150 s, 75 s, and 75 s, respectively (the same observation is also included in the data set presented in Section 2.2.2). Later, Joshi et al. (2017) observed the source with the Mount Abu 1.2 m telescope and the Physical Research Laboratory (PRL) near-IR Imager/Spectrograph, and reported near-IR magnitudes on 2017 March 20 (MJD 57832) of $J = 14.3$, $H = 14.0$, and $K_S = 13.7$, with typical errors of 0.1 magnitude, for a total integration time of 15, 15, and 17.5 minutes, respectively. These magnitudes are consistent with those derived in our analysis of the REM data during the 2016–2017 outburst, before the subtraction of the contribution from the nearby 2MASS star (see Section 2.2.2 for a detailed discussion).

We also use the historical IR data of the source from its mini-outburst in 1994, taken on 1994 July 8 (MJD 49541) in the *J* and *K* filters of 16.2 ± 0.3 and 15.5 ± 0.3 , respectively (Chaty et al. 2002), especially for the spectral energy distribution study (see Section 3.3).

2.3. Archival Swift/UVOT Observations

We gathered publicly available Swift UV/Optical Telescope (UVOT) pointing observations of the source during its entire outburst from the NASA/HEASARC data center. We used the pipeline processed images and obtained the magnitude of the

source using the `uvotsource` HEASOFT routine, with an aperture of 5 arcsec centered on the source. An empty region close to GRS 1716–249 was chosen as the background region. We select only those 81 pointings where the source flux estimate is at least 5σ above the sky background. Although the UVOT observations of this source were available in all the filters, most of the significant and usable detections were found to be in the V ($0.546 \mu\text{m}$), B ($0.439 \mu\text{m}$), and U ($0.346 \mu\text{m}$) bands, with a smaller amount of detections in the $UVW1$ ($0.260 \mu\text{m}$) bands.

Similar to the optical flux values, we de-reddened the UV data. We use the absorption column density $N_{\text{H}} = (0.70 \pm 0.01) \times 10^{22} \text{ cm}^{-2}$, reported in Bassi et al. (2020), the generic relation between optical extinction and hydrogen column density (Foight et al. 2016), and the wavelength-dependent extinction terms using the extinction curve of Mathis (1990).

2.4. Archival Radio Detections

We use the radio observations of the source during its outburst with the Karl G. Jansky Very Large Array (VLA; 5.25, 7.45, 8.8 and 11.0 GHz), Australia Telescope Compact Array (ATCA; 5.5 and 9.0 GHz) and Australian Long Baseline Array (LBA; 8.4 GHz) as reported in Bassi et al. (2019) and Atri et al. (2019). Radio detections of the source are available for 2017 February 9 and 11 (MJD 57993 and 57995), April 22 (MJD 57865), August 12 and 13 (MJD 57977 and 57978). We use all the radio detections for which more than one quasi-simultaneous (within 24 hr) optical/UV measurement is available, to study the broadband spectral energy distribution (SED) of the source (see Section 3.3).

2.5. Archival Data from X-Ray Telescopes

We acquired X-ray monitoring data of GRS 1716–249 from the Swift/BAT and Swift/XRT telescopes. Swift/BAT has observed the source almost daily from 2016 December 1 (MJD 57723) in the 15–50 keV flux range. We extracted the daily average light-curve data of this source from the Swift/BAT transient monitor³⁸ (Krimm et al. 2013). To convert the count-rates to flux, we used the hydrogen column density $N_{\text{H}} = (0.70 \pm 0.01) \times 10^{22} \text{ cm}^{-2}$ and a photon index of $\Gamma = 1.68 \pm 0.01$, as reported in (Bassi et al. 2020). Swift/XRT observations were made every few days between 2017 January 28 (MJD 57781) and 2017 October 20 (MJD 58046), mostly in the window timing mode, with target IDs 34924 and 88233 (see Table 1, of Bassi et al. 2019, for a detailed observation log). We used the on-line Swift/XRT products generator³⁹ (Evans et al. 2007, 2009) to extract the 2–10 keV count rate of GRS 1716–249 from each XRT observation, after correcting for instrumental artefacts.

GRS 1716–249 was also observed with Nuclear Spectroscopic Telescope Array (NuSTAR) during the 2016–2017 outburst. We calculate the NuSTAR flux density of the source using `NUPIPELINE V0.4.6` in HEASOFT V6.25, with the calibration file version v20171002. Both Science Mode and Spacecraft Mode data were considered. The flux was calculated in the Swift BAT energy band (15–50 keV) using the best-fit spectral models provided in Jiang et al. (2020). A relativistic

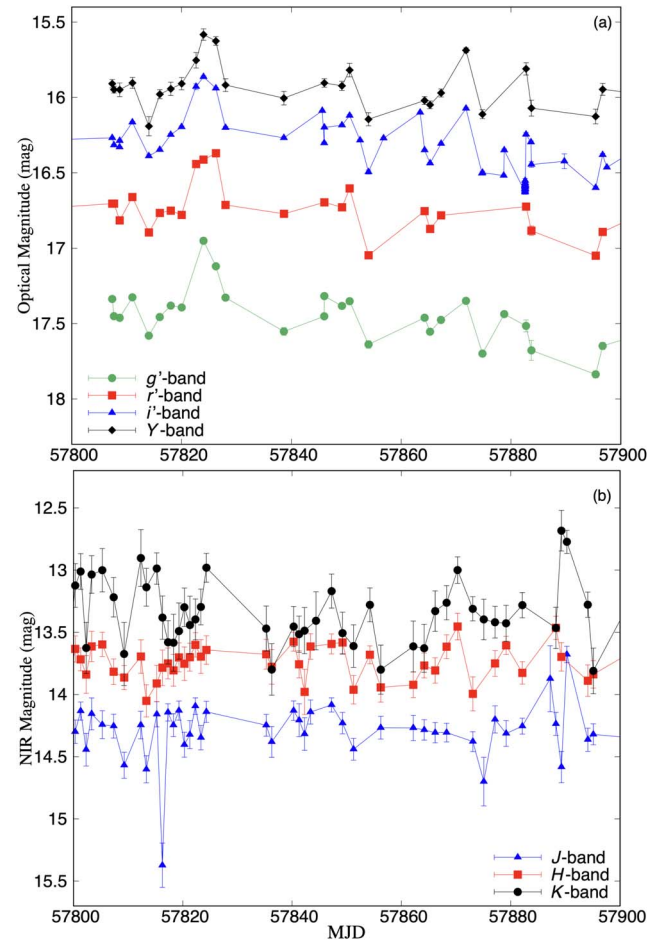


Figure 3. Zoom-in of the (a) optical and (b) near-IR light curve of GRS 1716–249 during the peak of the 2016–2017 outburst to show the optical/IR variability.

disk reflection model with a variable disk density parameter was used (Ross & Fabian 2007). Detailed descriptions of spectral modeling can be found in Jiang et al. (2020).

We also gathered daily X-ray monitoring data of GRS 1716–249 from MAXI/GSC⁴⁰ (Matsuoka et al. 2009) in the 2–20 keV range covering the complete outburst.

3. Results

3.1. Multiwavelength Light Curve

The light curves of the entire outburst are plotted in Figure 2 including data in near-IR (REM), optical (LCO and Gaia), UV (UVOT), and X-ray (NuSTAR, Swift XRT, and BAT, MAXI) wavelengths.

The first optical detection of GRS 1716–249 during the 2016–2017 outburst was obtained by LCO on MJD 57781, when the optical magnitude was already bright, with $i' = 15.97 \pm 0.01$. Since that time, we regularly monitored the source in i' , g' , r' , and Y bands until its optical emission faded back to quiescence. There are also some scattered observations taken in the B and V bands. A zoom-in of the optical light curve during the peak of the outburst between 2017 January 28 and May 27 (MJD 57800–57900) is shown in Figure 3(a). The general trend of the LCO light curve is an almost constant

³⁸ <https://swift.gsfc.nasa.gov/results/transients>

³⁹ https://www.swift.ac.uk/user_objects/

⁴⁰ http://maxi.riken.jp/top/lc_bh.html

plateau in all the optical bands during the outburst, until ~ 2017 May 27 (MJD 57900), followed by a slow and steady decline to quiescence until 2017 October 20 (MJD 58046). The same behavior was also observed in the Gaia optical light curve in the G band. At the end phase of the decline, we find a small amplitude optical brightening of the source, with i' magnitudes changing from 17.80 ± 0.01 on 2017 October 7 (MJD 58033) to 17.45 ± 0.01 on October 15 (MJD 58041) and then again back to 18.10 ± 0.01 on October 18 (MJD 58044).

The optical/UV light curves obtained with Swift/UVOT in the U , B , V , $UVW1$, $UVW2$, and $UVM2$ bands, show a similar outburst profile as the LCO and Gaia light curves. The complete outburst, including the decay toward quiescence, is well covered by the U -band data. The brightening observed in optical wavelengths during the decline of the outburst is not evident in the UV data.

The near-IR REM light curve is approximately constant, with some scatter and flickering, until 2017 June 21 (MJD 57925). A zoom-in of the near-IR light curve during the peak of the outburst is shown in Figure 3(b). After MJD 57925, the flux starts to show a decreasing trend in all bands until ~ 2017 September 4 (MJD 58000), when the flux experiences a plateau that lasts until the end of the observations. This behavior is similar to that of the higher energy light curves.

The X-ray light curves in both the hard (Swift/BAT and NuSTAR) and the soft (Swift/XRT and MAXI) energy ranges follow the morphology of the near-IR/optical light curve, indicating a correlated behavior, which is explored in detail in Section 3.4.

3.2. Optical/IR Variability

3.2.1. Optical Variability

Figure 3(a) shows the zoom-in of the optical light curve during the peak of the outburst. On longer timescales, the four LCO optical filters (g' , r' , i' , and Y band) are clearly correlated. We also took higher cadence optical observations on 2017 May 9 (MJD 57882; 15 detections in ~ 17.5 minutes with a time resolution of ~ 75 s) of the source with LCO i' band. The optical fractional rms deviation in the flux on such short timescales (minutes; i.e., a frequency range of 0.0010–0.013 Hz) during the hard state, evaluated following the method described in Vaughan et al. (2003) and Gandhi et al. (2010), is found to be $1.3\% \pm 0.4\%$, reflecting on a very weak variability.

The observed rms is substantially lower than the optical fractional rms of BHXBs like GX 339–4 and Swift J1357.2–0933 in the hard state and V404 Cyg in the flaring state, which are $\sim 5\%$ – 20% on similar and shorter timescales (Gandhi 2009; Gandhi et al. 2010; Cadolle Bel et al. 2011; Gandhi et al. 2016; Paice et al. 2019). The variability seen in GRS 1716–249 is similar to the lower optical fractional rms values of $\sim 3\%$ – 5% seen in the hard accretion states of Swift J1753–0127, XTE J1118+480 and MAXI J1535–571 (Gandhi 2009; Hynes et al. 2009; Baglio et al. 2018). Such variability is also observed in the soft accretion states of GX 339–4 and GRO J1655–40 (Hynes et al. 1998; O’Brien et al. 2002; Cadolle Bel et al. 2011), when the accretion disk dominates the emission.

3.2.2. Infrared Variability

Figure 3(b) shows the zoom-in of the near-IR light curve during the peak, where the source is observed to be varying by

~ 1 magnitude. We also observe a possible small amplitude (~ 0.5 – 0.6 mag) flare happening in J and K bands between MJD 57887 and 57891. However, no corresponding activity is observed in H band, and the lack of time-resolved data during these days makes it difficult to study this event further. The fractional rms deviation in the infrared flux of GRS 1716–249 during the peak of the outburst on longer timescales (days/weeks; a frequency range of 5.8×10^{-6} – 8.7×10^{-8} Hz), after removing the contribution from the blended star, is measured to be $20.69\% \pm 2.34\%$, $10.92\% \pm 4.86\%$, and $34.43\% \pm 4.24\%$ in the J , H , and K bands, respectively. Hence GRS 1716–249 is variable in the near-IR band. Although the coverage of the outburst in the mid-IR range is scarce, the detections and the upper limits (see also Table 1 and Section 2.2.1) also point to a variable mid-IR emission, with the flux density spanning from < 1.4 mJy to 3.2 ± 0.6 mJy at $8.7 \mu\text{m}$.

A similar increase of fractional rms deviation in the flux toward longer wavelengths in the optical/IR wavelength range, is also seen in other BHXBs. For example, the rms is often 10% – 20% or higher in the near-IR regime in the hard accretion states, as seen in sources like XTE J1550–564, GX 339–4, and MAXI J1820+070 (Curran & Chaty 2013; Vincentelli et al. 2018; Tetarenko et al. 2021). In the mid-IR regime, the fractional rms increases further with, for example, rms $\sim 15\%$ – 22% in MAXI J1535–571 at a similar time resolution, which supports a jet origin to the variability on these timescales (Baglio et al. 2018). In XTE J1118+480, the spectrum of the rms variability is consistent with a power-law distribution of spectral index $\alpha = -0.6$ from optically thin synchrotron radiation, spanning near-IR to X-ray (Hynes et al. 2003, 2006). In the hard accretion state of MAXI J1820+070, the fractional rms (in a larger integrated frequency range; 10^{-4} – 50 Hz) decreases monotonically with increasing wavelength, from tens of percent in the optical/near-IR, to 2% – 8% at radio frequencies (Tetarenko et al. 2021). Other timing properties such as the frequency of the break in the power spectrum was also seen to vary smoothly with wavelength from optical to radio, with time lags between bands increasing at longer wavelengths. One interpretation is that, although the fractional variability increases from optical to IR due to an increase in the jet contribution, the fractional rms drops again as it approaches radio wavelengths, because the variability in the jet-dominated bands gets more smoothed out by the larger size scale of the emitting region at the longer wavelengths.

3.3. Spectral Energy Distribution

We construct the optical/UV spectra as well as the broadband SEDs of GRS 1716–249 in the hard (Figure 4(a)) and hard-intermediate states (Figure 4(b)), to illustrate the peculiar multiwavelength characteristics of the source. In Figure 4, we plot the optical/UV spectra of GRS 1716–249 in both the hard (Figure 4(a)) and hard-intermediate states (Figure 4(b)) of the outburst. We use quasi-simultaneous observations obtained within 24 hr, and convert the magnitudes to de-reddened fluxes as described in Section 2.1 for optical LCO magnitudes and Section 2.3 for archival Swift/UVOT observations. In both the hard-intermediate and hard states, the SEDs are found to be smooth up to the $UVW1$ -band, with a shallow peak around the g' band.

We use the available information to constrain the intrinsic optical/UV spectral index by fitting the function $S_\nu \propto \nu^\alpha$, where S_ν is the flux density, ν is the frequency, and α is the

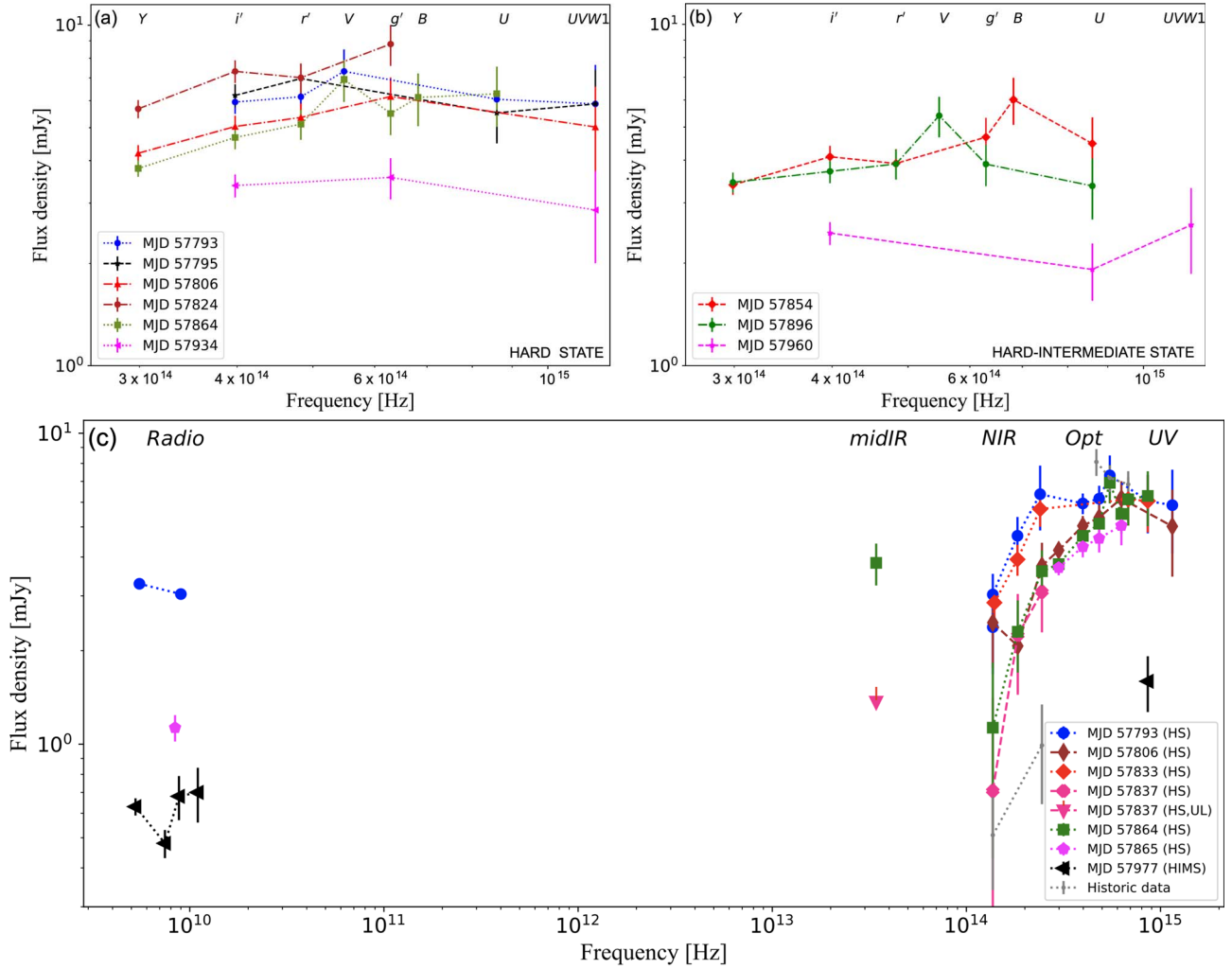


Figure 4. De-reddened optical/UV spectra of GRS 1716–249 during (a) the hard and (b) the hard-intermediate state of the outburst, when quasi-simultaneous (within 24 hr) observations were available. (c) The de-reddened radio/mid-IR/near-IR/UV spectrum when quasi-simultaneous (within 24 hr) data were available. The mid-IR to radio spectral index measured from the VISIR mid-IR detection on MJD 57864.4 and LBA radio detection at 8.4 GHz on MJD 578865.7 is found to be $\alpha = 0.13 \pm 0.03$. The mid-IR upper limit on MJD 57837 in the J8.9 filter is plotted as an inverted triangle, to show the mid-IR variability of the source. We also plot for reference the historical optical (MJD 49268, della Valle et al. 1994) and near-IR (MJD 49541, Chaty et al. 2002) SEDs from its discovery outburst in 1993/1994 (in gray dotted lines).

spectral index. We obtain an average $U-i'$ spectral index of $\alpha_{U-i'} = -0.1 \pm 0.3$ across the spectra. Generally, a negative slope ~ -0.7 (e.g., Gandhi et al. 2011) is expected if there is a jet present with an optically thin synchrotron spectrum dominating the near-IR/optical regime. This value can be even more negative, as seen in cases like Swift J1357.2–0933 where the quiescent optical/mid-IR SED has a power-law index of -1.4 , arising from a weak jet (Shahbaz et al. 2013). Although optically thick, self-absorbed synchrotron emission from a jet can produce slope ~ -0.1 , there are only a few cases in which such emission extends to higher frequencies like optical (e.g., Russell et al. 2013; Maitra et al. 2017). A positive slope SED is expected (with spectral index ~ 1) if the optical emission is dominated by the blackbody from the outer accretion disk (e.g., Hynes 2005). For a viscously heated disk, $\alpha \sim 0.3$ is expected, turning to a steeper slope $0.3 < \alpha < 2.0$ at lower frequencies (e.g., Frank et al. 2002). Very often, a combination of all the processes can result in an intermediate slope.

For comparison, during the hard state, the spectrum constructed for GRS 1716–249 on 2017 February 22 (MJD

57806), has an $\alpha_{Y-g'} \sim 0.5$, while, during the hard-intermediate state on 2017 April 11 (MJD 57854), we find $\alpha_{Y-B} \sim 0.7$ (See Figures 4(a) and (b)). This suggests the optical spectra are probably dominated by an accretion disk, but it is unlikely for the UV/optical emission to solely originate from the Rayleigh–Jeans part of a single-temperature blackbody spectrum.

To investigate the issue further and disentangle the emission processes in the optical and UV regime, we include the available IR and radio data and construct the broadband spectrum (see Figure 4(c)) and the SED (see Figure 6) of GRS 1716–249 with quasi-simultaneous (within 24 hr) optical (with LCO), near-IR (with the Mount Abu 1.2 m telescope and REM), mid-IR (with VISIR), and radio (with ATCA, LBA, and VLA) data. The broadband spectrum has a positive slope in the near-IR regime, which flattens in the optical, and gets fainter in the UV wavelengths. We fit the spectrum on MJD 57864 with a single-temperature blackbody curve (see Figure 5), and find that the NIR/optical/UV part of the spectrum is qualitatively well represented by a blackbody model with a temperature $\sim 10,500 \pm 200$ K, while the mid-IR emission is comparatively brighter. This suggests that the overall shape of the IR/optical/

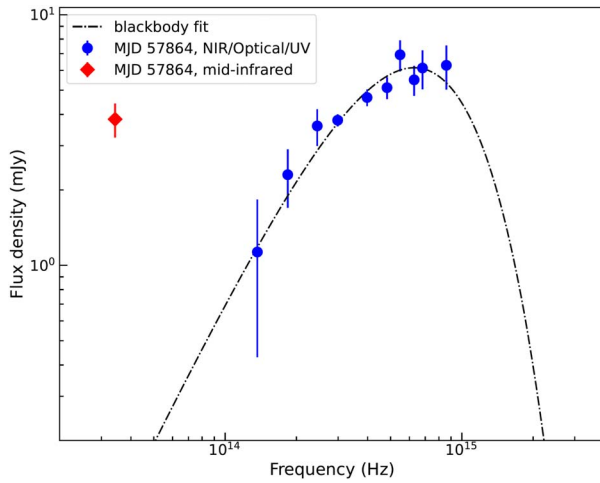


Figure 5. The quasi-simultaneous, de-reddened NIR/optical/UV spectrum of GRS 1716-249 on MJD 57864 (blue circles). Superimposed is the fit of the spectra with a single-temperature blackbody (black line). We also overplot the quasi-simultaneous mid-IR detection of the source for comparison (red diamond). We show that the NIR/optical/UV part of the spectrum is qualitatively well represented by the single-temperature blackbody, while the mid-IR emission is comparatively brighter probably due to an additional contribution from the jet.

UV spectra together are as expected for the outer accretion disk. The steeper slope in the NIR is the Rayleigh–Jeans limit of the blackbody with the lowest temperature. The fainter UV emission suggests that the viscous disk does not dominate in these wavelengths (as the UV emission does not keep rising with $\alpha \sim 0.3$). Instead, the irradiated disk most likely dominates the emission, as a peak is seen around the g' band, with UV flux densities being slightly fainter. This is similar to seen in other BHXBs where the irradiation bump peaks in the optical, with the UV slightly fainter (e.g., Hynes 2005). The historical optical (taken in 1993) and near-IR (taken in 1994) data from the discovery outburst, plotted in Figure 4(c) for a comparison with the current outburst, show a similar brightness

profile in optical, although not as flat as the recent data. In the near-IR wavelengths, although it was fainter during the historical outburst, it shows a similar shape with a positive slope.

The single mid-IR detection of the source, obtained on 2017 April 21 (MJD 57864), is significantly brighter than what is expected from the disk alone (see Figures 5 and 6), and can probably be attributed to synchrotron emission from a compact jet during the outburst. The mid-IR to radio spectral index measured from the VISIR mid-IR detection on MJD 57864.4 and the LBA radio detection at 8.4 GHz on MJD 57865.7 (a separation of 1.3 d) is found to be $\alpha = 0.13 \pm 0.03$. This is slightly more positive than (but consistent with to within $<2\sigma$), the reported radio spectral indices of $\alpha = -0.15 \pm 0.08$ and $\alpha = -0.07 \pm 0.19$, at the beginning (2017 February 9, MJD 57793.8) and close to the end of the outburst (2017 August 12, MJD 57977.3), respectively (Bassi et al. 2019). Therefore, the radio to mid-IR spectrum is consistent with a flat or slightly inverted spectrum coming from a compact jet. We also estimate the spectral index between the mid-IR detection and quasi-simultaneous X-ray spectrum as $\alpha = -0.26$. If the mid-IR emission arises from optically thin synchrotron, then its extrapolation to X-ray is much fainter than the observed X-ray power-law index, which implies that the synchrotron jet does not contribute much to the X-ray flux.

3.4. Multiwavelength Correlations

Another tool for disentangling the emission processes in BHXBs during outburst is multiwavelength correlations. We study the quasi-simultaneous multiwavelength correlation of GRS 1716-249, using de-reddened optical and UV fluxes as a function of the soft X-ray (2–10 keV) fluxes from Swift/XRT, and hard X-ray (15–50 keV) fluxes from Swift/BAT and NuSTAR; whenever the X-ray fluxes are obtained within a day of the optical or UV observations.

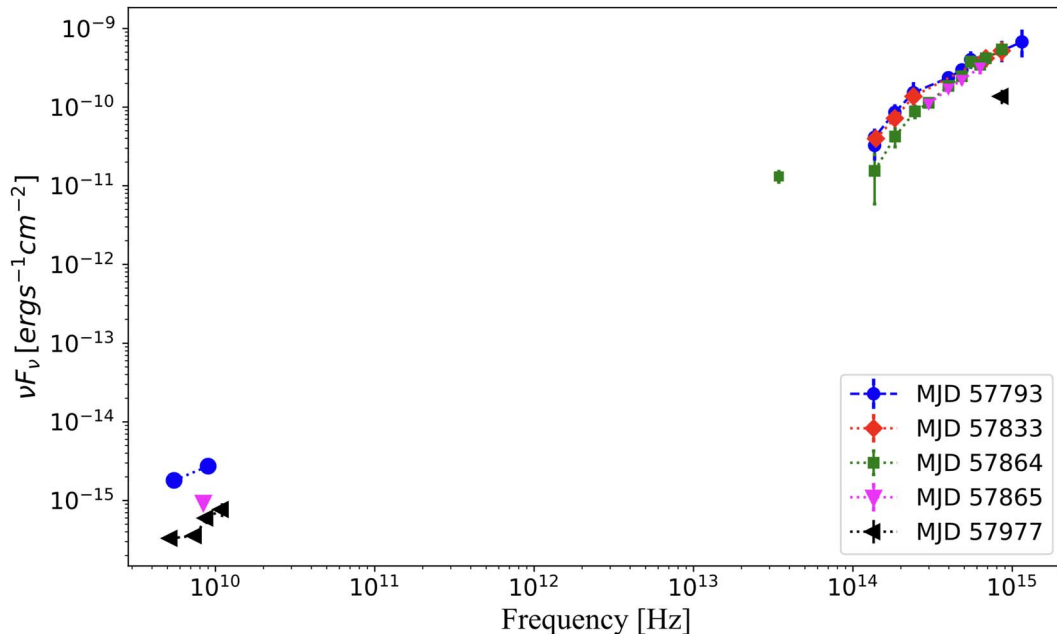


Figure 6. De-reddened broadband SED of GRS 1716-249 on the five days during the hard state when quasi-simultaneous (within 24 hr) infrared, optical, radio, and UV detections were available. The SEDs presented here are from the hard state, except on MJD 57977 (shown in black triangles) when the source was in the hard-intermediate state.

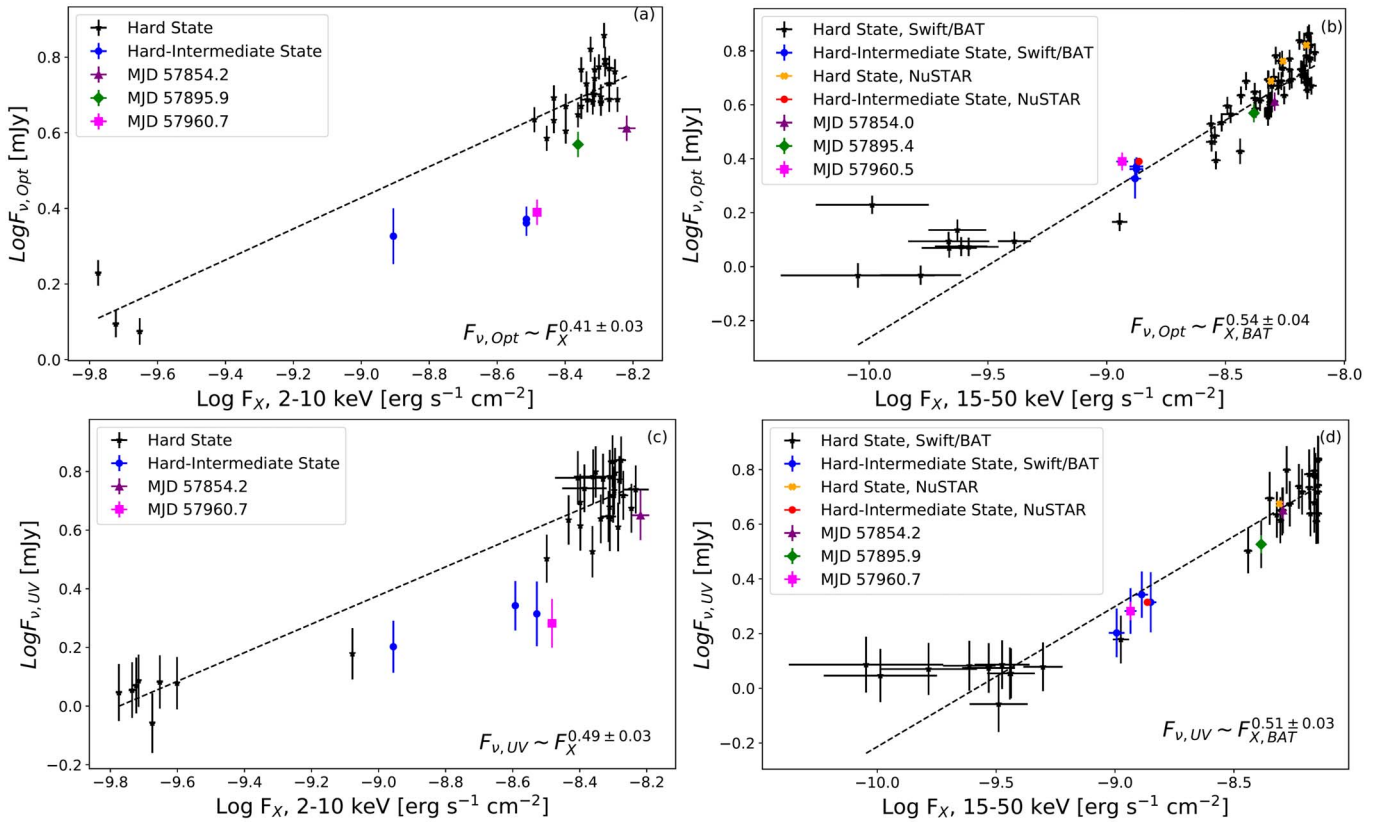


Figure 7. Optical/X-ray correlation for GRS 1716–249. While the top two plots show the correlation with optical flux densities in the i' band obtained from the LCO telescopes, the bottom plots use the U -band flux densities obtained with Swift UVOT. We use quasi-simultaneous (within 24 hr) X-rays taken either from Swift/XRT in the 2–10 keV range (for the left plots), or from Swift/BAT and NuSTAR in the 15–50 keV (in the right plots). The black dashed lines show the best fit using the orthogonal distance regression method of least squares, and the slope is mentioned in the plot. The hard state values with Swift XRT and BAT are shown in black stars, the hard state values with NuSTAR are shown in orange crosses. The hard-intermediate state values with Swift XRT and BAT are shown in blue circles, and with NuSTAR in red circles. The softest points during the three softening events (Bassi et al. 2019) are shown in colored symbols, where the MJD values are indicated.

3.4.1. Optical versus X-Ray Correlations

For the optical versus soft X-ray (2–10 keV) correlation study, we use Swift/XRT flux in the 2–10 keV range for X-rays, and de-reddened optical i' -band flux density (as the i' band had the best coverage among all optical filters). We choose all the points for which we have quasi-simultaneous data (i.e., data obtained within 24 hr; see Figure 7(a)). While the hard state values follow one single correlation, the hard-intermediate state values (shown in the plot as colored points with non-circular symbols, where the MJD values are indicated) are generally seen to lie on the lower side of the correlation. This is in agreement with previous studies where comparatively less optical emission is observed during the state transition and soft state (e.g., Jain et al. 2001; Corbel & Fender 2002; Homan & Belloni 2005; Russell et al. 2006; Coriat et al. 2009). Generally, this is thought to be due to a weak jet component to the optical emission, which usually fades during the transition from the hard to hard-intermediate state (e.g., Cadolle Bel et al. 2011; Baglio et al. 2018) and recovers when a BHXB returns to the hard state (e.g., Corbel et al. 2013; Kalemci et al. 2013; Russell et al. 2013). Another reason could be a weak disk-blackbody component which can contribute toward the X-ray luminosity in the 2–10 keV energy range during the hard-intermediate state (Capitanio et al. 2009; Alabarta et al. 2020).

The correlation is found to be significant (Pearson correlation coefficient = 0.84, p value = 2.5×10^{-10}). The best-fit

slope for the correlation in hard state using the orthogonal distance regression method of least squares is 0.41 ± 0.03 . The observed slope suggests an X-ray irradiated accretion disk (van Paradijs & McClintock 1994), with possibly some contribution from the viscous disk (Russell et al. 2006). But we note that the scaling relation of van Paradijs & McClintock (1994) depends on an assumed geometrical configuration and is not as simple and straightforward. Recent studies have showed that the slope of the correlation can differ depending on the origin of the emission at different regimes (e.g., Coriat et al. 2009; Tetarenko et al. 2020), and irradiation from a hot dense accretion disk wind may also cause a slight distortion of the scaling relation (Cuneo et al. 2020, see also Section 4.1 for a detailed discussion).

In addition, we note that there is a slight hint of the correlation flattening at the fainter end of the luminosity ranges. As an alternative explanation, we attempted to fit the data with a broken power law (keeping the break luminosity as a free parameter). The correlation obtained were found to have a steeper slope (~ 1.1) at the brighter end, and a shallower slope (~ 0.2) at the fainter end, implying that the viscous disk could play a role at the lower luminosities (the break luminosity was found to be $\sim 2.5 \times 10^{-9} \text{ erg s}^{-1} \text{ cm}^{-2}$). A prominent role of the viscous disk in the fainter part of the outburst is also hinted at by our color evolution analysis (see Section 3.5).

The hard X-ray emission (15–50 keV) of the source follows a power-law correlation with the optical flux. To check this correlation, we used hard X-ray data in the 15–50 keV range

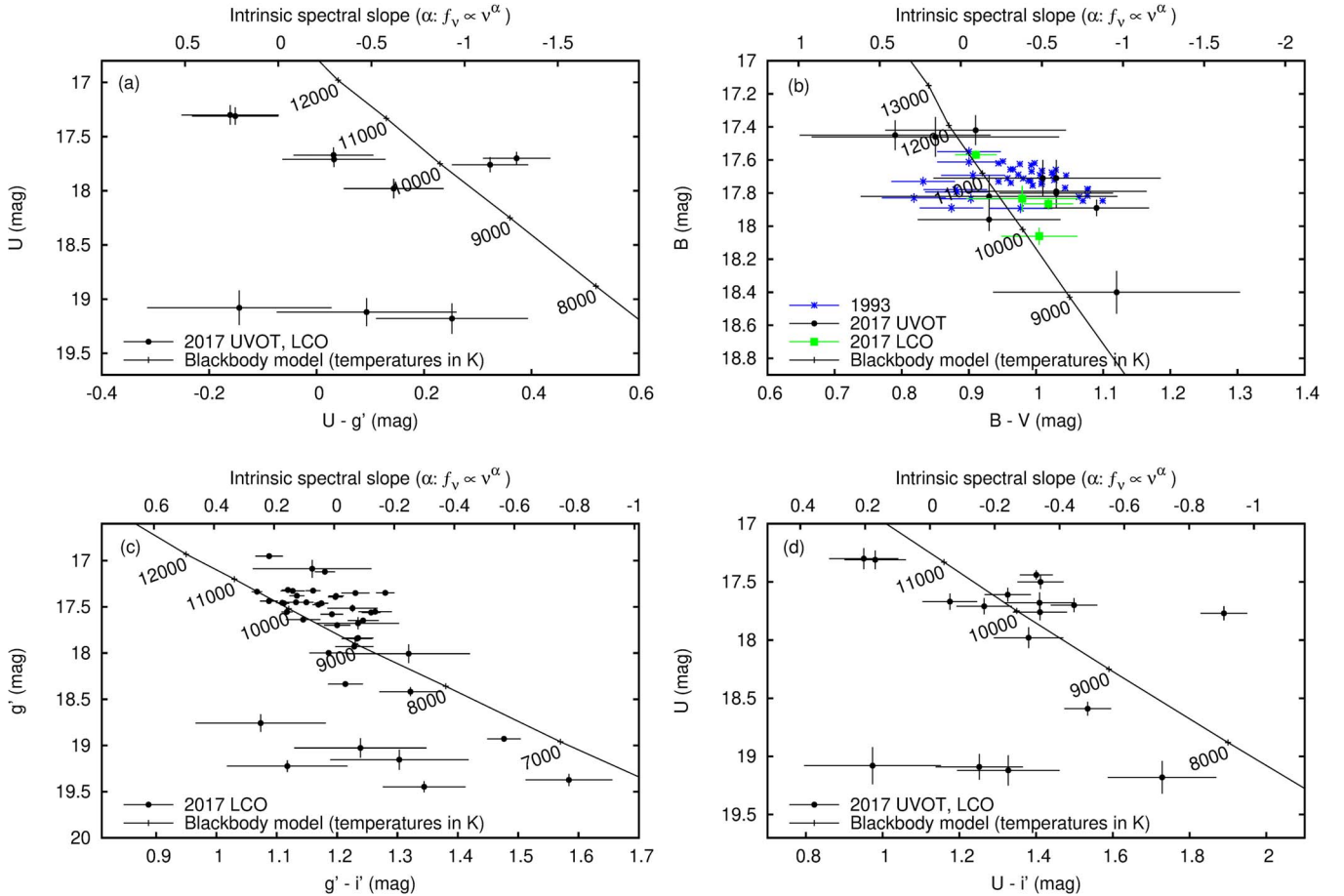


Figure 8. Color–magnitude diagrams, adopting four different filter combinations. For each combination, the bluer filter is on the y-axis. Bluer colors (greater spectral index) are to the left, redder colors (lower spectral index) are to the right. A simple model of a single-temperature blackbody heating up and cooling, used to approximate emission from reprocessing on the disk, is denoted by the black line labeled with the temperature values, in each panel (see text). (a) The $U - g'$ CMD is the combination showing the shortest wavelengths; the reprocessing model is a poor approximation of the data, the viscously heated disk likely plays a strong role at the fainter epochs. (b) The $B - V$ CMD also includes some data from the 1993 outburst (della Valle et al. 1994; Masetti et al. 1996); the reprocessing model approximates most of the data well (brightest epochs in both outbursts). (c) The $g' - i'$ CMD is the combination with the longest wavelengths; the reprocessing model is close to the data at bright epochs but not during the outburst fade, when the viscous disk likely dominates. (d) The $U - i'$ CMD shows the widest wavelength range; again reprocessing can describe most of the brightest epochs, not the fainter epochs.

from Swift/BAT telescope and NuSTAR with de-reddened i' -band flux density obtained from LCO (see Figure 7(b)). The correlation with a power-law index of $\sim 0.54 \pm 0.04$ is found to be significant (Pearson correlation coefficient = 0.93, p value = 1.2×10^{-13}). The difference between hard state and hard-intermediate state here is subtle, as probably the hard X-ray flux is also fading slightly in this state compared to the hard state, such that the optical and the hard X-ray flux are both fainter, maintaining the correlation.

3.4.2. U-band versus X-Ray Correlations

The U -band/soft X-ray correlation is plotted in Figure 7(c) with U -band detections from the UVOT telescope, and simultaneous soft X-ray data from Swift/XRT in the 2–10 keV energy range. The correlation is significant (Pearson correlation coefficient = 0.94, p value = 2.6×10^{-12}) and the power-law index of the UV/X-ray correlation is found to be $\sim 0.49 \pm 0.03$, which is consistent with an irradiated accretion disk (van Paradijs & McClintock 1994). Similar to the optical/X-ray correlation, the hard-intermediate state values were seen to have weaker U -band emission in comparison to the hard state. A correlation was also observed between the U band and

the hard X-ray emission (15–50 keV, from Swift/BAT telescope and NuSTAR, see Figure 7(d)), with high significance (Pearson correlation coefficient = 0.95, p value = 1.2×10^{-15}), and a similar slope of $\sim 0.51 \pm 0.03$. There is a hint of the correlation flattening at the lower-luminosity end, as also seen in the case of the optical/X-ray correlations. But due to the lack of fainter data points, and the large uncertainties associated with it, a conclusive result regarding a broken power law can not be obtained. But we note that a shallower correlation could arise due to the emergence of a viscous disk at the end of the outburst (see also Section 3.5).

3.5. Color–magnitude Diagram

The color–magnitude diagrams (CMDs) are plotted in Figure 8, using four different filter combinations using the i' , g' , U , B , and V filters. We adopt the single-temperature blackbody model of Maitra & Bailyn (2008), described in detail in Russell et al. (2011) to study the color evolution of X-ray binaries during outbursts, which approximates the emission from the X-ray-irradiated outer accretion disk. A color change is expected due to the evolving temperature of the

irradiated disk, which is assumed to have a constant emitting surface area. While, at high temperatures, the optical emission is expected to originate in the Rayleigh–Jeans tail of the blackbody, at lower temperatures, it originates near the peak of the blackbody curve. The blackbody temperature of the model depends on the intrinsic color and the interstellar extinction.

The normalization of the model depends on the accretion disk radius (estimated using the known orbital period, mass of the companion star, and the mass of the black hole from the literature), the distance to the source, inclination angle, the disk-filling factor, disk warping, and the fraction of disk that is reprocessing the X-rays. As many of these parameters are not certain, we choose a value of the normalization that best describes the trend in the data. In particular, we fix the normalization using the $B-V$ CMD (see Figure 8(b)) as this filter combination has the most data, and is less affected by the jet emission (if present), being from the bluer wavelengths. We find that the data do not completely agree with the single-temperature blackbody model, which indicates that more than one component is likely to be present. The disk temperature was roughly seen increasing from $\sim 7,000$ K to $\sim 12,000$ K, as expected during outbursts when hydrogen in the disk is typically ionized.

We find that the data in the $B-V$ CMD, which includes some data from the 1993 outburst (data from della Valle et al. 1994; Masetti et al. 1996), generally follows the expected trend between color and magnitude, with scatter of ± 0.1 mag in color. These data were from the brightest epochs in both outbursts. We adopt the same normalization that this provides to the other three filter combinations. We note that there is an uncertainty on the normalization due to the scatter in the color, but it should not be larger than ~ 0.1 mag in color. Assuming that the same normalization can be applied to the other filter combinations, we can investigate deviations from the blackbody model as a function of wavelength combination. For these filter combinations, we find that the brightest epochs show data close to the blackbody model, but at lower luminosities there are significant deviations, whereby the observed color is much bluer, in some epochs, compared to model expectations (see Figure 8 caption). The spectral index in these faint data points, instead of decreasing to a value of $\alpha \sim -1$ at $g' > 19$ mag, diverges away from the model, to values of $\alpha = 0 - 0.3$. A spectral index of $+1/3$ is expected for the overlapping radii of a viscously heated disk (e.g., Frank et al. 2002). It may be that reprocessing on the disk becomes less important at these lower luminosities, revealing the viscously heated disk as the outburst fades.

If the viscous disk, with $\alpha = +1/3$, is responsible for the deviations from the model, one would expect this to affect the shorter wavelengths more than the longer wavelengths, since this component rises at shorter wavelengths. This seems to be the case, with a color deviation of $\sim 0.7-1.0$ mag in the $U-g'$ and $U-i'$ CMDs, and ~ 0.5 mag in the $g'-i'$ CMD. The companion star could start to contribute to the optical emission at low fluxes, but we consider this to be unlikely to cause the observed deviations because (a) the star would have to be rising toward the blue, requiring it to be a more massive companion than is likely in this LMXB, and (b) the fluxes during the decay are still a couple of magnitudes above the quiescent level (see below), so the star is unlikely to dominate the emission. Optical emission from the viscous disk also has a shallower relation with the X-ray flux, compared to reprocessing, and this is

hinted at in Figure 7 whereby the correlation slopes seem to appear shallower at lower luminosities compared to higher luminosities.

In the $g'-i'$ CMD (see Figure 8(c)), some of the brightest epochs show data that deviate from the blackbody model in the opposite sense; some data points are redder than the blackbody model by up to 0.2 mag in color. This is less prominent in the other CMD filter combinations. Since $g'-i'$ is the combination with the longest wavelengths, this is likely due to an additional component that is redder than the disk component, and which only makes a contribution at high luminosities. It is also variable; some data points are close to the blackbody model and so this redder component seems to vary in time. This is therefore probably the jet making a weak contribution to the i' band, since we know that the jet makes a stronger contribution at longer wavelengths in the infrared (Section 3.3) and it is variable (Section 3.2).

3.6. Long-term Monitoring and Quiescent Magnitude

The only report of any optical quiescent magnitudes of GRS 1716–249 in the literature is a single weak constraint of $B \sim 21.0-21.5$ mag (della Valle et al. 1993). The source was not detected with Gaia in quiescence, and it only appears in EDR3 after the new outburst data were included (see Section 2.1.2). This provides a 20.7 mag limit in the G band (Brown et al. 2016).

We have been monitoring GRS 1716–249 in quiescence with LCO (mostly using the 2 m Faulkes Telescope South) for the last 15 yr, since 2006 February 3 (MJD 53769; see Section 2.1.1 for details). The monitoring continues past the data we report on here through 2022 February. During quiescence, all the measurements obtained with XB-NEWS are forced-photometry points centered at the position of GRS 1716–249. On visual inspection of the quiescent data, we find that, in most of the images, the target is not visible at its expected position, and the quiescent magnitudes from XB-NEWS could be contaminated by emission from a brighter source very close to ($\sim 2''$ away from) the transient within the aperture, and a faint star $1''.6$ away from the X-ray binary (see Figure 1), making them unreliable.

To obtain a reliable quiescent optical magnitude, we select all the LCO images with good seeing ($< 1''.6$) and perform aperture photometry at the source position using an aperture size of ~ 1 arcsecond in order to exclude the flux from the nearby stars and obtain the quiescent magnitude. The finding chart in quiescence obtained from the image with the best seeing ($\sim 0''.82$) is shown in the right panel of Figure 1. We find uncontaminated detections of the source at 13 epochs during quiescence spanning a range of 10 yr (2011 May–2021 May, see Figure 9). There is a slight variation during quiescence, with the i' -band magnitudes ranging from 21.04 ± 0.17 (MJD 59137.4) to 21.88 ± 0.28 (MJD 58344.5). By combining all seven detections with seeing $< 1''.1$, we find the quiescent i' -band magnitude $= 21.39 \pm 0.15$ mag. The position of the source in quiescence is consistent with that measured from outburst data. The quiescent magnitude does not appear to change (within errors of the variations) before versus after the 2016–2017 outburst. We also rule out there being any long mini-outbursts after the 2017 outburst.

In the near-IR wavelengths, the source is not detected with 2MASS during quiescence (Rout et al. 2021), inferring an upper limit of 15.8 mag for the J band, 15.1 mag for the H

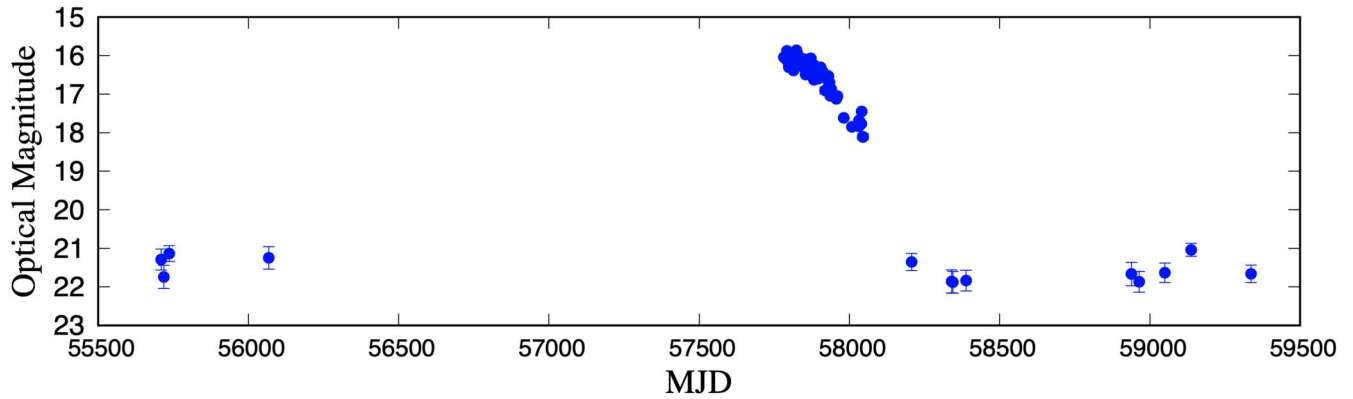


Figure 9. The long-term (~ 10 yr) light curve of GRS 1716–249 in the i' band with LCO from 2011 May (MJD 55709.39) to 2021 May (MJD 59336.68), showing the quiescent variability of the source.

band, and 14.3 for the K band (Skrutskie 2006). From archival J -band images of the field taken during quiescence on 1999 July 5 and 7 (MJD 51364 and 51366) with the SOFI instrument at the New Technology Telescope (NTT; La Silla, Chile), we find a 3σ upper limit of the source of $J > 18.8$ mag, while the nearby southern star was found to have magnitudes of $J = 15.38 \pm 0.05$ mag (see Section 2.2.2). There is a mention of probable near-IR quiescent magnitudes of GRS 1716–249, as Chaty et al. (2002) detected the source in J , H , and K bands with the 2.2 m La Silla Telescope (ESO, Chile) on 1997 July 19 (MJD 50648) when it was expected to be in quiescence. They tabulate the quiescent magnitudes of the source as $J = 19.4 \pm 1.2$; $H = 19.2 \pm 1.0$; $K = 18.3 \pm 1.0$. But they note that the source was not detected on 1998 July 6 (MJD 51000), and caution that observations with more powerful telescopes are needed to confirm the quiescent magnitudes.

4. Discussion

Compared to the origins of X-ray or radio emission in a BHXB, the origin of the optical and near-IR emission is much less understood. Many physical processes could potentially contribute to the emission at these wavelengths, including X-ray reprocessing by the outer accretion disk (Cunningham 1976; Vrtilek et al. 1990), intrinsic thermal emission from a viscously heated outer accretion disk (Shakura & Sunyaev 1973; Frank et al. 2002), synchrotron emission originating from a steady compact jet during the hard state (e.g., Jain et al. 2001; Markoff et al. 2001; Corbel & Fender 2002; Buxton & Bailyn 2004; Russell et al. 2006; Kalemci et al. 2013; Saikia et al. 2019) and sometimes in transitional states (e.g., Fender et al. 2004; van der Horst et al. 2013; Koljonen et al. 2015; Russell et al. 2020), a hot inner flow during the hard state (e.g., Veledina et al. 2013), and the companion star during quiescence (e.g., Casares & Jonker 2014). In this section, we explore the various emission processes contributing to the optical/UV fluxes of GRS 1716–249 using information from the methods mentioned previously, and discuss their implications on the system parameters, especially the distance to the source.

4.1. Optical/UV/IR Emission Mechanism

We study the optical/UV as well as broadband SEDs of GRS 1716–249 with quasi-simultaneous (within 24 hr) data, and find that they show a flat spectrum at optical/UV wavelengths (with a slight peak in the optical), with a positive

slope in the near-IR regime, suggesting that the optical/UV emission mainly originates from a multi-temperature accretion disk. The optical/UV emission is near the peak of the blackbody from reprocessing. The fainter near-IR emission compared to optical is consistent with the Rayleigh–Jeans tail of the blackbody from the outer disk. The mid-IR emission on one date is comparatively brighter than what is expected from the disk alone. Such excess of emission in the IR regime is seen in many BHXBs (e.g., XTE J1550–564, Jain et al. 2001; 4U 1543–47, Buxton & Bailyn 2004; H1743–322, Chaty et al. 2015; XTE J1650–500, Curran et al. 2012; GX 339–4, Corbel & Fender 2002; Homan et al. 2005), generally associated with a compact jet. Along with being above the disk model, the mid-IR emission is also highly variable (see Table 1), and the radio to mid-IR spectrum is slightly inverted (with an index of $\alpha = 0.13 \pm 0.03$), which are typical signs of jet emission from BHXBs. The broadband spectral fitting performed by Rout et al. (2021) also shows that an irradiated accretion disk dominates the ultraviolet and optical emission. They report an IR excess compared to what is predicted by the irradiated disk model, and interpret it as due to the presence of a jet. Similarly, Bassi et al. (2020) fitted their broadband SED with the irradiated disk model *diskir* to describe the contribution of the accretion flow emission, which accounts for the irradiation of the outer disk and the reprocessing of the X-ray photons in the optical/UV band.

The slope of the optical/X-ray correlation also reveals the dominant emission mechanism of the accretion disk. For an X-ray reprocessing accretion disk, the slope of the correlation is theoretically expected to be ~ 0.5 (van Paradijs & McClintock 1994). But we note that the theoretical value can be slightly different if there are extra contributions coming from additional emission components like irradiation from a disk wind, and can have a much larger range of slopes depending on which wavelength is used and whether the optical emission is coming from the Rayleigh–Jeans tail (RJ) or closer to the peak of the blackbody disk (Coriat et al. 2009; Shahbaz et al. 2015; Tetarenko et al. 2020). On the other hand, for a viscously heated disk the slope of the correlation is expected to have a wavelength-dependent value ~ 0.3 (Russell et al. 2006) and, for an optically thick jet, the expected slope is ~ 0.5 – 0.7 (Corbel et al. 2003; Russell et al. 2006). For GRS 1716–249, the best-fit power-law correlations indicate the optical/X-ray slope to be 0.41 ± 0.03 (see Section 3.4). This value is consistent with the X-ray irradiated accretion disk (van Paradijs & McClintock 1994), with additional contribution from the viscous disk,

which could lower the value of the fitted slope from the theoretical value of ~ 0.5 for irradiation (Russell et al. 2006). An X-ray irradiated accretion disk with optical emission coming from the peak of the blackbody, is also favored by recent studies that find that the expected slope in the hard state can range from 0.13 (optical flux at RJ tail) to 0.33 (flux in the multicolour disk blackbody) for a viscously heated disk, and from 0.14 (RJ tail) to 0.67 (disk) for X-ray reprocessing with an isothermal disk (for a detailed calculation, see Coriat et al. 2009; Tetarenko et al. 2020;). For cases like GRS 1716–249, where the outer disk temperature rises to $\sim 10,000$ K in outburst (see Figure 8), the optical flux is found at the spectral transition between the RJ tail and the multicolor blackbody (Russell et al. 2006), and hence the optical/X-ray slope of 0.41 ± 0.03 is consistent with the scenario of X-ray reprocessing. Similar values of power-law correlations have also been seen in other X-ray binaries like XTE J1817–330 (0.47 ± 0.03 , Rykoff et al. 2007), GX 339–4 (0.44 ± 0.01 , Coriat et al. 2009), and GS 1354–64 (~ 0.4 – 0.5 , Koljonen et al. 2016). On the other hand, many sources like Swift J1357.2–0933 (Armas Padilla et al. 2013), Swift J1910.2–0546 (Saikia et al. 2022), SAX J1808.4–3658 (Patruno et al. 2016), and Cen X-4 (Baglio et al. 2022) show a significantly shallower correlation (~ 0.1 – 0.3). A slightly steeper correlation (~ 0.56) is seen for V404 Cyg (Bernardini et al. 2016; Hynes et al. 2019; Oates et al. 2019), probably arising from contamination in optical fluxes from jet contribution. From our multiwavelength correlation and spectral energy distribution analysis, we can rule out a significant optical emission component arising from a jet, in GRS 1716–249.

This is also supported by our variability studies. Generally, sources with strong optical/IR variability on short (seconds to minute) timescales are known to have a strong jet contribution, and the variability is stronger at longer wavelengths where the disk makes a smaller contribution (Gandhi 2009; Gandhi et al. 2010; Baglio et al. 2018; Tetarenko et al. 2021). Disk variability is driven by changes in the mass-accretion rate, which happen on the viscous timescale (days to weeks) for the viscously heated disk, and shorter (minute) timescales for reprocessing on the disk surface, if the X-rays have strong variability (with the reprocessing being smeared). The lack of strong variability in our optical data on short (minute) timescales, along with the presence of correlated variability on longer (days) timescales, suggests that the disk is producing the optical emission, and the contribution of the synchrotron jet emission at optical wavelengths is low in GRS 1716–249. The emission at near-IR wavelengths is dominated by the accretion disk, with a weak and variable jet component contributing toward the K band in a few epochs. At mid-IR wavelengths, we find evidence for a highly variable jet component as suggested by the variable emission and the mid-IR to radio spectral index.

In addition to this, we investigated the color evolution of the source during its outburst. Our CMD analysis shows that the observed optical data mostly agrees with the single-temperature blackbody model (at least at higher luminosities), with a scatter of ± 0.1 mag in color. This agreement supports the finding that the optical emission is originating mainly from a disk with varying temperature. The disk temperature varied between ~ 7000 K to $\sim 12,000$ K, which is optimal for ionizing hydrogen in the disk. At the brighter epochs in the CMD filter combination with the longest wavelengths ($g'-i'$), we found that the data are slightly redder and brighter than what is expected

from the disk model, with possibly some contribution coming from a jet. At the fainter epochs, we found significant deviations of the data from the reprocessing model, where the observed color was much bluer, shifting the spectral index from $\alpha = 0$ to $+0.3$ (which is expected in a viscously heated disk, Frank et al. 2002).

It is also worth considering the possibility of optical or IR emission from the hot flow. In this scenario, synchrotron emission from overlapping components of the hot flow contribute to the optical emission (Veledina et al. 2013). We have found that the optical spectrum is well described by a multi-temperature disk, with the RJ tail in the IR (Section 3.3). The irradiation peak is detected, and there is low short-term variability (Section 3.2). These characteristics, along with the behavior in the optical/X-ray correlation and the CMDs, strongly favor a disk origin. In addition, Cuneo et al. (2020) detected variable, double-peaked emission lines from hydrogen and helium, in the optical spectrum. These lines originate in the rotating accretion disk, and P-Cygni profiles were also detected from a disk wind. The hot-flow model predicts strong short timescale optical variability (stronger in the optical compared to the IR because variations are amplified closer to the black hole, and the IR synchrotron emission in the hot flow originates at larger radii) and a flat optical spectrum with a downturn at longer wavelengths (Veledina et al. 2013). We find stronger, high amplitude variability in the IR compared to optical, with the mid-IR flux density being higher than the optical on one date. The spectrum, emission lines, and variability properties are therefore not consistent with expectations from the hot flow. The hot-flow model predicts a lower flux in the IR because the synchrotron-emitting region is physically limited by the inner edge of the accretion disk. So, while the optical is dominated by the disk, the mid-IR must be dominated by the jet, not the hot flow.

4.2. Constraints on the System Parameters

We also conduct a comparative study of the quasi-simultaneous optical/X-ray emission of GRS 1716–249 against a large sample of black hole and neutron star LMXBs in Figure 10, with data taken from Russell et al. (2006, 2007). Both these classes of LMXBs are known to show different correlations, with the neutron star LMXBs being around 20 times optically fainter than black hole LMXBs (Russell et al. 2006), for reasons discussed in Bernardini et al. (2016). Assuming the previously estimated distance of 2.4 ± 0.4 kpc (della Valle et al. 1994) is correct, GRS 1716–249 is found to be much more optically faint (or X-ray bright) compared to other BHXB samples (see the left panel in Figure 10); in fact, at this distance GRS 1716–249 agrees more with the neutron star track in the global optical/X-ray correlation plot.

4.2.1. BH Nature of GRS 1716–249

A BH nature of the source was first inferred by Masetti et al. (1996), who derived a lower limit for the compact object mass of $>4.9 M_{\odot}$ from the super-hump period of 14.7 hr. Super humps generally appear in disks with viscous-dominated emission, where the luminosity variations are caused by viscous dissipation associated with tidal deformation of the disk when it reaches the 3:1 resonance radius. We have shown in Section 4.1 with several lines of reasoning that the disk emission in GRS 1716–249 during outburst is dominated by

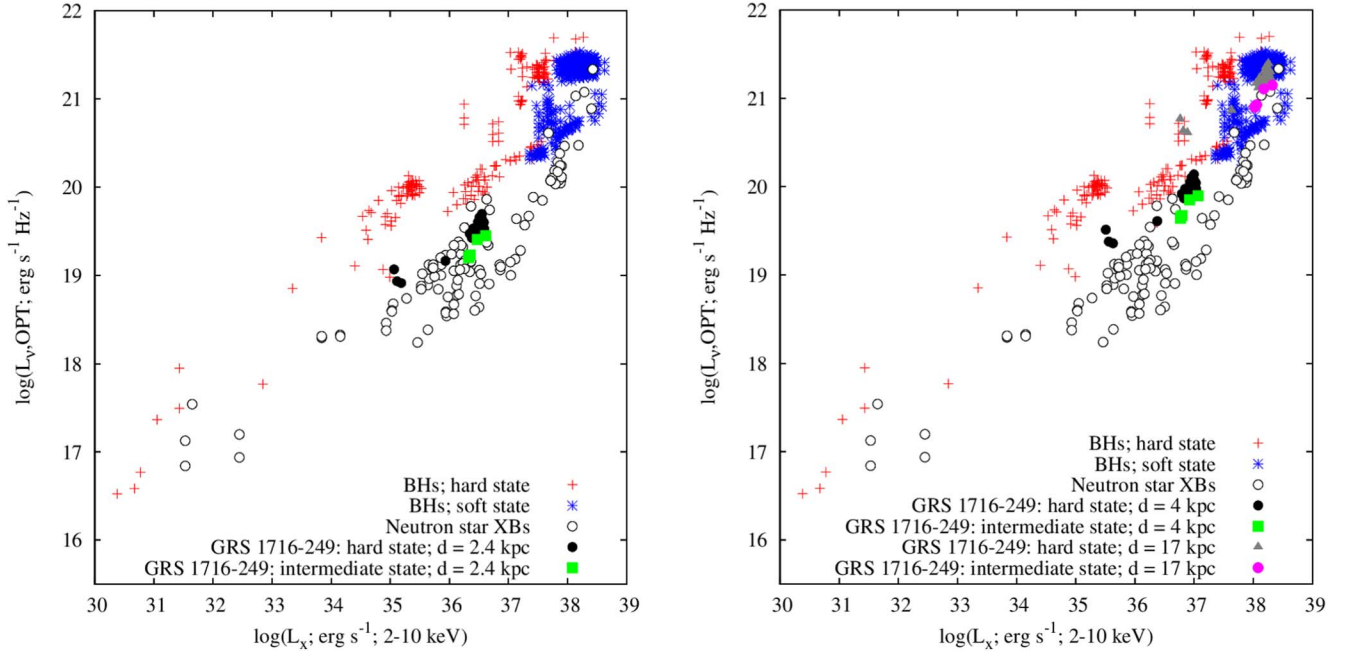


Figure 10. Optical/X-ray correlation for GRS 1716–249 and samples of black hole and neutron star LMXBs, assuming the distances of 2.4 kpc (left; literature value), and the upper and lower bounds of the range that is empirically consistent with other BHXBs; 4–17 kpc (right).

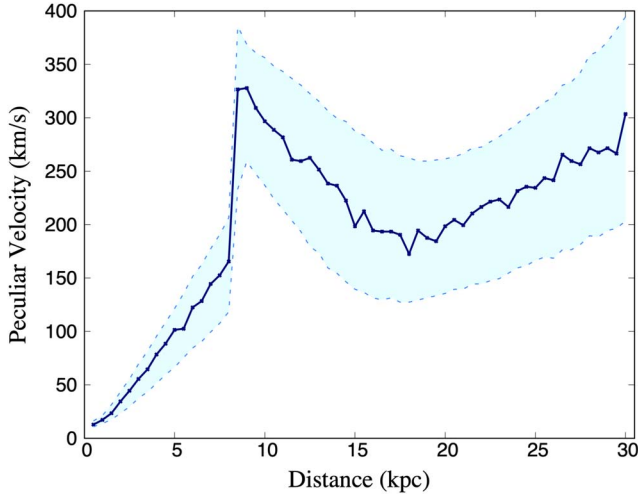


Figure 11. Expected peculiar velocity (v_{pec}) of GRS 1716–249 for a range of possible distances over 0.5–30 kpc. The shaded region bound by the two dashed lines represents the 1σ scatter. The kinematics of the system favor distances of $\lesssim 8$ kpc; as for BH systems, the natal kick probability distribution ranges only up to $\sim 150 \text{ km s}^{-1}$ (Mandel & Muller 2020).

X-ray irradiation. Such systems can have orbital modulations due to irradiation, rather than (or in addition to) super humps (see the discussion in Haswell et al. 2001), especially when part of the optical variability comes from the irradiated face of the donor star. The super-hump variability can be dominant at high orbital inclinations when the donor star to BH mass ratio is low and the donor star is shielded from irradiation, but optical modulation can be expected when the ratio is higher (see the discussion in Torres et al. 2021). As it is not clearly known whether the optical variability reported by Masetti et al. (1996) was a super hump or an irradiation effect, we cannot use it as a reliable constraint to the BH mass.

Masetti et al. (1996) also noted that a massive primary is expected from the very long decay time of the X-ray light

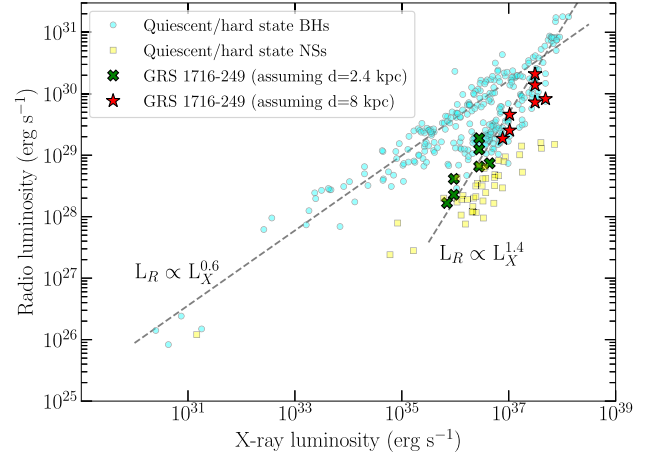


Figure 12. Radio/X-ray luminosity correlation plot of GRS 1716–249 with quasi-simultaneous data from Bassi et al. (2019), and a large sample of black hole and neutron star LMXBs with data made available by Bahramian et al. (2018). The X-ray luminosities are in the 1–10 keV energy range, while the radio luminosities are taken in ~ 5 and 9 GHz. The green crosses depict the position of the source assuming the distance of 2.4 kpc (literature value), and the red stars represent the position when a greater distance (in this case, 8 kpc) is assumed.

curve. Later, Tao et al. (2019) studied three quasi-simultaneous NuSTAR and Swift data sets of the system in its hard-intermediate state, and assuming a distance of 2.4 kpc, constrained the upper limit for the compact object mass to be $< 8.0 M_{\odot}$, at a 90% confidence level. Chatterjee et al. (2021) also used X-ray spectral analysis of the source during outburst to suggest a BH nature of the compact object. They fitted the X-ray spectra of GRS 1716–249 with the physical two-component advective flow (TCAF) model, keeping the mass of the primary as a free parameter, and constrained the mass of the compact object in the range of $4.5\text{--}5.9 M_{\odot}$, but the values obtained are highly model dependent and very unlikely to be a realistic range. The lack of Type I bursts during the outburst

Table A1
 Faulkes/LCO Optical Detections (AB Magnitudes) of GRS 1716–249 during the 2016–2017 Outburst

<i>i</i> band			<i>g'</i> band			<i>r'</i> band		
MJD	Magnitude	Error	MJD	Magnitude	Error	MJD	Magnitude	Error
57781.76280	16.046	0.008						
57790.37413	16.107	0.009				57790.37282	16.563	0.010
57792.11238	15.881	0.011				57792.11104	16.365	0.010
57794.34359	16.089	0.017				57794.34227	16.553	0.016
57794.65647	16.086	0.007						
57795.72785	16.039	0.015				57795.72654	16.419	0.040
57798.35717	16.306	0.012				57798.35586	16.725	0.014
57798.64443	16.278	0.005						
57807.36263	16.269	0.005	57807.36557	17.336	0.007	57807.36849	16.704	0.005
57807.69145	16.316	0.006	57807.69308	17.451	0.017	57807.69460	16.704	0.007
57808.72058	16.329	0.005	57808.73102	17.461	0.010	57808.73395	16.815	0.008
57808.72806	16.287	0.006						
57811.03827	16.165	0.006	57811.04126	17.325	0.011	57811.04423	16.660	0.006
57814.03003	16.389	0.011	57814.03302	17.580	0.015	57814.03905	16.895	0.008
57816.02459	16.347	0.006	57816.02759	17.456	0.009	57816.03362	16.766	0.006
57818.01929	16.247	0.007	57818.02229	17.380	0.010	57818.02832	16.751	0.007
57820.01393	16.196	0.007	57820.01691	17.393	0.010	57820.02297	16.779	0.006
57822.65082	15.929	0.019				57822.65975	16.442	0.011
57824.00293	15.863	0.008	57824.00592	16.951	0.021	57824.01197	16.412	0.009
57826.25255	15.940	0.060	57826.25548	17.120	0.016	57826.26145	16.370	0.007
57828.00147	16.201	0.009	57828.00446	17.328	0.018	57828.01048	16.713	0.010
57838.64016	16.268	0.009	57838.64180	17.552	0.026	57838.64500	16.772	0.014
57845.62141	16.088	0.003						
57845.97092	16.303	0.007	57845.97392	17.452	0.010			
57846.00164	16.199	0.006	57846.00463	17.317	0.008	57846.01070	16.696	0.006
57849.21821	16.184	0.006	57849.22115	17.382	0.012	57849.22709	16.728	0.007
57850.60261	16.120	0.008	57850.60557	17.351	0.022	57850.61154	16.603	0.009
57852.49929	16.284	0.006						
57854.04275	16.495	0.014	57854.04514	17.638	0.025	57854.05076	17.046	0.022
57856.79728	16.271	0.009						
57863.46871	16.100	0.004						
57864.27177	16.349	0.005	57864.26883	17.461	0.007	57864.27766	16.754	0.005
57865.27192	16.437	0.006	57865.26898	17.554	0.007	57865.27784	16.872	0.005
57867.27192	16.307	0.005	57867.26897	17.476	0.009	57867.27783	16.782	0.006
57871.81080	16.073	0.007	57871.80948	17.348	0.014			
57874.73148	16.504	0.005						
57874.80092	16.499	0.010	57874.79960	17.699	0.021			
57878.68604	16.518	0.005						
57878.77927	16.350	0.008	57878.78106	17.437	0.012			
57882.75055	16.246	0.013	57882.75196	17.515	0.040	57882.75494	16.724	0.018
57883.63992	16.297	0.009						
57883.72140	16.445	0.018	57883.72281	17.678	0.066	57883.72579	16.884	0.031
57889.71699	16.423	0.049						
57895.43395	16.600	0.011	57895.43536	17.836	0.023	57895.43833	17.050	0.014
57896.70059	16.381	0.010	57896.70235	17.648	0.024	57896.70641	16.892	0.015
57897.46580	16.464	0.005						
57904.49230	16.304	0.008	57904.49406	17.561	0.013	57904.49704	16.761	0.009
57907.45315	16.562	0.006						
57910.77233	16.412	0.009						
57919.69822	16.905	0.085						
57929.48416	16.612	0.010	57929.48535	17.844	0.023			
57930.47042	16.535	0.007						
57930.62906	16.670	0.017	57930.63024	18.007	0.100			
57932.39149	16.813	0.012	57932.39266	17.998	0.030			
57934.10396	16.701	0.014	57934.10530	17.930	0.028			
57937.29423	17.043	0.010						
57939.53233	16.873	0.030						
57956.59849	17.121	0.018	57956.60008	18.335	0.023	57956.60167	17.640	0.019
57956.62583	17.073	0.015	57956.62725	18.418	0.049	57956.62854	17.552	0.025
57960.53634	17.055	0.010						
57981.30615	17.617	0.013						
58008.43489	17.847	0.020						
			58029.04037	19.041	0.047			

Table A1
(Continued)

<i>i</i> band			<i>g'</i> band			<i>r'</i> band		
MJD	Magnitude	Error	MJD	Magnitude	Error	MJD	Magnitude	Error
58031.37832	17.838	0.029						
58032.41498	17.685	0.051						
58033.41110	17.803	0.035						
58035.37890	17.792	0.030						
58039.39175	17.770	0.030	58039.39461	19.373	0.065			
58041.00927	17.456	0.019	58041.01225	18.928	0.020			
58044.39425	18.108	0.031	58044.39704	19.448	0.061			
58045.74268	18.106	0.079	58045.74565	19.224	0.062			

(This table is available in machine-readable form.)

despite the presence of hydrogen (as suggested by the $H\alpha$ lines, Cuneo et al. 2020) also provide strong evidence against an NS accretor. Moreover, Tao et al. (2019) show that good quality NuSTAR X-ray spectra of the source in the intermediate states can be fitted by BH models. In addition to the previous evidence, the X-ray timing properties of GRS 1716–249 also suggest that the compact object of the system is a BH. Chatterjee et al. (2021) report different power density spectra (PDS) of GRS 1716–249 in their Figure 4, all of which show a strong decline from ~ 3 Hz to 10 Hz. This behavior is more typical of BH systems since the PDS of BHXBs show a strong decline at frequencies above 10–50 Hz (Revnivtsev 2000). NS systems, on the contrary, can show variability up to 500–1000 Hz. The lack of X-ray pulsations and kilohertz QPOs in the PDS (typical signatures of neutron star systems), the presence of type-C and type-B QPOs in the PDS of GRS 1716–249 (Chatterjee et al. 2021), and the strong decline of the power spectra below 10 Hz all reinforce the identification of the compact object as a BH.

If GRS 1716–249 is indeed a black hole, then the discrepancy shown by GRS 1716–249 with respect to other BHXBs in the global optical/X-ray correlation space could have two possible explanations. Either the source is intrinsically much more optically faint than what has been observed in other BHXBs at a given X-ray luminosity, or it is located much further away than was previously thought.

4.2.2. Distance to GRS 1716–249

The original distance estimate of 2.4 ± 0.4 kpc is based on a comparison of the source to other X-ray binaries with data from a few decades before (della Valle et al. 1994). They argued that the lower limit on the distance is expected to be ~ 2 kpc from the equivalent width of the NaD absorption lines. To constrain the upper limit, the peak optical brightness was compared to other BHXB outbursts known at the time (della Valle et al. 1994). Since then, a distance of 2.4 ± 0.4 kpc has been used by various studies concerning GRS 1716–249. Later Hynes (2005) notes that one should be cautious about using such a method to constrain the upper limit on the distance. It has now become clear that BHXB outbursts can peak at different luminosities, from close to the Eddington limit, down to $\sim 10^{36}$ erg s $^{-1}$ or less (e.g., the Very Faint X-ray Binaries, or mini-outbursts; Heinke et al. 2015; Zhang et al. 2019). Moreover, the historic peak optical brightness of LMXBs during outburst used by della Valle et al. (1994) was based on a compilation that neither corrected for orbital period, nor performed sorting of neutron stars versus black holes (van

Paradijs 1981). In light of all these arguments we do not consider the formerly estimated upper limit of 2.8 kpc as a reliable constraint.

Masetti et al. (1996) had discovered optical modulations in the source with a prominent period of ~ 14.7 hr, and found that the secondary star in the system should be substantially brighter than claimed by della Valle et al. (1994). To explain this discrepancy, they suggested that either the distance of 2.4 ± 0.4 kpc has been underestimated, or the secondary is a slightly evolved late-type star.

In addition to the previous arguments, we also find that a higher value of distance is expected from the state transition luminosity distribution of the source (e.g., Maccarone 2003; Kalemci et al. 2013; Vahdat Motlagh et al. 2019). It has been observed that BHXBs transit from the soft state to the hard state at luminosities between 0.3% and 3% of the Eddington luminosity (Kalemci et al. 2013), with a mean value of $1.9\% \pm 0.2\%$ (Maccarone 2003). The state transition luminosity has been used to estimate the distances to many BHXB sources (e.g., Homan et al. 2006; Miller-Jones et al. 2012). Although GRS 1716–249 did not go to a soft state, we use the luminosity during transition from the final hard/intermediate state to the hard state (MJD 57978, Swift/XRT flux 9.25×10^{-10} erg s $^{-1}$ cm $^{-2}$ at 2–10 keV) to estimate the distance. Assuming a BH of mass $7 M_{\odot}$, $1.9\% \pm 0.2\%$ Eddington luminosity and a bolometric correction factor of 2 relative to the Swift/XRT band, we obtain a probable distance of 8.7 ± 0.5 kpc for the source. For a more conservative range of 0.3%–3% Eddington luminosity (Kalemci et al. 2013), the distance range is found to be 3.46–10.94 kpc.

Moreover, for a distance of 2.4 kpc, the inner disk radius depending on the inclination angle is $r_{\text{in}} \sim 15$ km (see Figure 6 of Bassi et al. 2019), which is very unusual for a BH disk spectrum; while a more plausible value of $r_{\text{in}} > 50$ km is obtained for distances $d > 8$ kpc. An underestimated distance could also explain the discrepancy we see for this source with respect to other BHXBs in the optical/X-ray correlation plots (see Figure 10). From our global correlation comparison, we find that, for a distance of 4 kpc and less, the data are more consistent with being a neutron star, and for distances more than 4 kpc, the data are more consistent with a BH.

We also place a conservative upper limit on the distance as 17 kpc from the global optical/X-ray correlation plot (see Figure 10), as for a greater distance, the source would be the most X-ray-luminous BHXB, probably exceeding the Eddington limit (depending on the black hole mass). The proper motion estimate of the source is $\sim 4.65 \pm 1.12$ mas/year, and

Table A2
REM Near-IR Detections of GRS 1716–249 during the 2016–2017 Outburst

<i>J</i> band			<i>H</i> band			<i>K</i> band		
MJD	Magnitude	Error	MJD	Magnitude	Error	MJD	Magnitude	Error
57792.32435	14.190	0.108	57792.32820	13.552	0.103	57792.33073	13.034	0.176
57793.32431	14.270	0.121	57793.32817	13.616	0.122	57793.33068	13.462	0.207
57794.32440	14.079	0.074	57794.32832	13.586	0.113	57794.33087	13.262	0.173
57795.33416	14.372	0.113	57795.33802	13.726	0.102	57795.34053	13.562	0.211
57796.37340	14.287	0.107	57796.37726	13.826	0.129	57796.37977	13.528	0.198
57798.30813	14.392	0.128	57798.30461	13.786	0.142	57798.30076	14.101	0.298
			57799.31212	13.873	0.112	57799.31462	13.600	0.240
57800.30831	14.299	0.094	57800.31216	13.633	0.105	57800.31468	13.123	0.176
57801.30816	14.133	0.072	57801.31200	13.717	0.092	57801.31452	13.011	0.143
57802.31356	14.443	0.132	57802.31742	13.839	0.151	57802.31990	13.626	0.205
57803.31346	14.155	0.128	57803.31733	13.613	0.122	57803.31984	13.035	0.151
57805.26872	14.242	0.112	57805.26521	13.597	0.097	57805.26137	13.001	0.174
57807.35268	14.254	0.096	57807.35655	13.817	0.103	57807.35907	13.218	0.158
57809.28189	14.569	0.105	57809.27835	13.864	0.097	57809.27451	13.674	0.254
57812.32570	14.245	0.110	57812.32958	13.695	0.134	57812.33209	12.903	0.228
57813.32666	14.602	0.109	57813.33053	14.051	0.129	57813.33304	13.137	0.152
57815.23916	14.159	0.101	57815.23564	13.911	0.146	57815.23180	12.987	0.126
			57816.26729	13.784	0.143	57816.26982	13.382	0.174
57817.28778	14.144	0.069	57817.29164	13.751	0.124	57817.29417	13.104	0.174
57818.28780	14.246	0.092	57818.29173	13.806	0.127	57818.29424	13.584	0.229
57819.28782	14.129	0.077	57819.29169	13.701	0.116	57819.29419	13.490	0.226
57820.29095	14.404	0.100	57820.29483	13.753	0.134	57820.29736	13.298	0.154
57821.29092	14.323	0.113	57821.29478	13.700	0.112	57821.29728	13.441	0.232
57822.30718	14.093	0.067	57822.31108	13.601	0.097	57822.31358	13.396	0.164
57823.32352	14.347	0.098	57823.31999	13.695	0.136	57823.31615	13.296	0.144
57824.32348	14.139	0.085	57824.31995	13.642	0.115	57824.31613	12.981	0.116
57835.26807	14.247	0.088	57835.27195	13.676	0.120	57835.27452	13.469	0.180
57836.27332	14.381	0.124	57836.27719	13.777	0.139	57836.27970	13.799	0.207
57840.28813	14.130	0.078	57840.28460	13.575	0.076	57840.28075	13.454	0.161
57841.28813	14.207	0.132	57841.28462	13.757	0.108	57841.28082	13.515	0.145
57842.28812	14.318	0.132	57842.28461	13.979	0.181	57842.28084	13.486	0.185
57843.37491	14.141	0.097	57843.37876	13.614	0.103			
						57844.38131	13.407	0.232
57847.22599	14.083	0.057	57847.22991	13.594	0.081	57847.23242	13.169	0.137
57849.22592	14.230	0.086	57849.22983	13.582	0.090	57849.23236	13.506	0.169
57851.24054	14.440	0.087	57851.24440	13.962	0.112	57851.24692	13.610	0.171
			57854.2229	13.680	0.071	57854.22542	13.279	0.136
57856.21885	14.267	0.091	57856.22273	13.943	0.119	57856.22526	13.800	0.197
57862.17564	14.269	0.101	57862.17210	13.922	0.103	57862.16824	13.614	0.204
57864.17594	14.284	0.082	57864.17243	13.767	0.100	57864.16858	13.628	0.192
57866.18714	14.307	0.082	57866.18362	13.807	0.101	57866.17983	13.329	0.163
57868.26877	14.306	0.075	57868.27263	13.615	0.096	57868.27513	13.262	0.137
			57870.27550	13.454	0.107	57870.27801	13.000	0.107
57873.07972	14.378	0.079	57873.07621	13.995	0.137	57873.07240	13.311	0.097
57875.08102	14.700	0.195				57875.07377	13.397	0.163
57877.13749	14.200	0.109	57877.13396	13.750	0.103	57877.13012	13.419	0.128
57879.16786	14.313	0.104	57879.16433	13.605	0.073	57879.16049	13.427	0.145
57882.13166	14.255	0.064	57882.12812	13.826	0.090	57882.12427	13.282	0.102
57887.22384	13.873	0.266						
57888.25770	14.236	0.092	57888.26169	13.464	0.093	57888.26419	13.465	0.166
57889.27466	14.583	0.127	57889.27853	13.697	0.114	57889.28102	12.682	0.164
57890.27447	13.678	0.066				57890.28084	12.772	0.093
57894.11317	14.363	0.093	57894.10966	13.889	0.126	57894.10581	13.278	0.101
57895.11313	14.320	0.084	57895.10962	13.838	0.110	57895.10578	13.810	0.183
57901.02803	14.343	0.108	57901.02453	13.686	0.139	57901.02068	13.318	0.124
57902.05513	14.335	0.091	57902.05157	13.808	0.122	57902.04774	13.726	0.148
57904.00570	14.414	0.097	57904.00218	13.655	0.097			
57905.06105	14.642	0.152	57905.05752	13.792	0.118	57905.05370	13.307	0.127
57906.06101	14.298	0.061	57906.05749	13.648	0.065	57906.05365	13.585	0.177
57907.06098	14.688	0.137	57907.05748	13.798	0.104	57907.05363	13.446	0.158
57908.07134	14.302	0.105	57908.06780	13.759	0.182	57908.06397	13.272	0.207
57909.07118	14.404	0.134	57909.06766	13.775	0.174	57909.06381	13.502	0.168
57910.07129	14.292	0.131	57910.06778	13.745	0.088	57910.06393	13.609	0.160

Table A2
(Continued)

<i>J</i> band			<i>H</i> band			<i>K</i> band		
MJD	Magnitude	Error	MJD	Magnitude	Error	MJD	Magnitude	Error
57911.07136	14.307	0.094	57911.06784	13.694	0.124	57911.06399	13.214	0.113
57913.03877	14.175	0.092	57913.03525	13.711	0.143	57913.03135	13.390	0.139
57915.05323	14.320	0.1195	57915.04971	13.616	0.104	57915.04584	13.730	0.176
57916.05831	14.516	0.107	57916.05479	14.055	0.130	57916.05095	13.552	0.145
57917.06366	14.461	0.116	57917.06013	13.888	0.112	57917.05629	13.406	0.135
57918.06363	14.461	0.116	57918.06012	13.750	0.111			
57922.04947	14.613	0.127	57922.04595	13.887	0.157	57922.04211	13.494	0.159
57924.15149	14.307	0.052	57924.15530	13.665	0.075	57924.15786	13.198	0.129
57925.23085	14.328	0.090	57925.23477	14.045	0.121	57925.23726	13.432	0.144
57933.12670	14.100	0.222						
57934.12671	14.568	0.113	57934.13060	13.948	0.103	57934.13311	13.564	0.182
57936.12677	14.318	0.156	57936.13060	14.159	0.180			
57937.14052	14.425	0.131	57937.13702	13.948	0.156	57937.13322	13.817	0.184
57938.30936	14.453	0.106	57938.30584	13.820	0.117	57938.30203	13.735	0.166
57949.33352	13.510	0.136	57949.33735	13.048	UL	57949.33980	12.613	UL
57951.09202	14.409	0.0815	57951.09588	14.209	0.170	57951.09841	13.755	0.236
57954.23148	14.267	0.102	57954.23537	13.714	0.140	57954.23789	13.132	0.142
57955.23142	14.241	0.102	57955.23530	13.741	0.140	57955.23779	13.273	0.221
57956.23142	14.368	0.116	57956.23534	13.872	0.128	57956.23785	13.737	0.182
57958.26998	14.480	0.129	57958.26647	14.104	0.180	57958.26263	13.693	0.195
57959.31483	14.342	0.082	57959.31134	14.032	0.130	57959.30750	13.640	0.173
57962.05381	14.313	0.145	57962.05775	13.856	0.146	57962.06027	13.403	0.168
57964.22435	14.578	0.099	57964.22824	13.685	0.100	57964.23077	13.800	0.221
						57967.02934	13.494	0.144
57969.96398	14.581	0.120	57969.96786	14.109	0.132	57969.97039	13.193	0.136
						57971.04542	13.458	0.197
57972.04106	13.162	0.050	57972.04494	15.766	UL	57972.04740	13.395	0.323
57973.24798	14.892	0.157	57973.25183	14.429	0.181	57973.25434	14.100	0.232
57974.24868	14.665	0.078	57974.25258	13.836	0.113	57974.25510	13.860	0.222
57982.22021	14.582	0.076	57982.22410	13.725	0.115	57982.22663	13.699	0.211
57983.24220	14.961	0.129	57983.24606	14.473	0.230	57983.24860	14.321	UL
57984.24218	15.228	0.220	57984.24604	13.968	0.160	57984.24853	13.734	UL
57987.21943	14.858	0.126	57987.22329	14.048	0.133	57987.22578	13.916	0.293
57990.09610	13.988	0.075	57990.09999	13.340	0.083	57990.10249	13.431	0.201
57991.22900	15.209	UL				57991.23530	14.023	UL
57994.21801	14.930	0.139	57994.22188	14.082	0.160	57994.22438	13.794	0.179
57998.21709	14.981	UL	57998.22096	14.139	UL			
58000.15082	14.856	0.121	58000.15469	14.359	0.165	58000.15717	13.678	0.159
58001.15070	15.253	0.207	58001.15456	14.207	0.135	58001.15705	13.673	0.156
58002.15071	14.783	0.209	58002.15457	14.781	UL	58002.15709	13.083	0.259
58003.15487	14.695	0.082	58003.15874	14.168	0.126	58003.16120	13.668	0.179
58004.15478	14.899	0.117	58004.15863	14.377	0.158	58004.16112	13.720	0.140
58007.12125	14.785	0.103	58007.12511	14.358	0.154	58007.12761	13.978	0.192
58008.12116	14.795	0.102	58008.12502	14.138	0.168	58008.12752	13.987	0.241
58010.12534	14.823	0.076	58010.12920	14.298	0.130	58010.13173	13.847	0.150
58011.12521	14.957	0.120	58011.12904	14.371	0.130	58011.13155	13.974	0.187
58012.12525	14.837	0.091	58012.12911	14.194	0.142	58012.13163	13.772	0.144
58017.08652	14.884	0.136	58017.09039	14.302	0.146	58017.09290	13.339	0.137
58019.06545	14.613	0.059	58019.06929	14.008	0.115	58019.07177	13.613	0.172
58021.05757	14.563	0.130	58021.06152	14.072	0.125	58021.06401	13.726	0.230
58022.05786	14.886	0.127	58022.06174	14.232	0.138	58022.06424	13.345	0.171
58024.08948	14.672	0.127	58024.09339	14.433	0.258	58024.09590	12.944	0.372
58025.08981	14.914	0.137	58025.09367	14.390	0.197			

Note. The Vega magnitudes before the subtraction of the contribution from the nearby star is reported here. If the source is not detected, the 3σ upper limit (UL) is reported.

(This table is available in machine-readable form.)

the potential kick velocity (after removing Galactic rotation) is $\sim 70\text{--}100\text{ km s}^{-1}$ for a distance $d = 2.4\text{ kpc}$ (Atri et al. 2019). We performed a simulation using all the standard assumptions of Gandhi et al. (2019) and the measured proper motions

assuming a radial velocity of -10 km s^{-1} (for further details, see Atri et al. 2019), and found that at any distance higher than 6 kpc , the space velocity of the source starts to exceed 100 km s^{-1} . At the Galactic center distance, the source peculiar

velocity increases to $\sim 150 \text{ km s}^{-1}$ (see Figure 11). On the other side of the Galaxy, however, median peculiar velocities are predicted to be between ~ 190 and 330 km s^{-1} . Such high velocities are not expected in BH systems, where the natal kick probability distribution ranges up to $\sim 150 \text{ km s}^{-1}$ with a root-mean-square kick of $\sim 60 \text{ km s}^{-1}$ (Mandel & Muller 2020). So the kinematics of the system favor distances of $\lesssim 8 \text{ kpc}$, suggesting that it is significantly closer than 17 kpc . We also note that the source had a failed-transition outburst and did not show a transition to the soft state (Bassi et al. 2019). Generally, the failed-transition outbursts reach lower peak X-ray luminosities than full outbursts (Tetarenko et al. 2016; Alabarta et al. 2021). For example, in the case of one of the best studied BHXB GX 339–4, the luminosity at which the hard-to-soft state transition occurs during a full outburst is $\sim 0.11 L_{\text{Edd}}$, and the luminosity during failed-transition outbursts are always equal to or lower than this value (Tetarenko et al. 2016). Assuming a similar behavior of $\sim 10\% L_{\text{Edd}}$ during the peak flux in the case of GRS 1716–249, a conservative mass of $7M_{\odot}$ results in a distance of 5.0 kpc , and adds additional support to a closer distance. From all the arguments stated above, we place a conservative upper limit of 17 kpc for the system, although our lines of evidence suggest a much lower value ($\sim 8 \text{ kpc}$).

From the global correlation plot and the list of reasoning mentioned, we constrain the distance of GRS 1716–249 to likely be in the range of $4\text{--}17 \text{ kpc}$ (see the right panel in Figure 10), with a most likely range of $\sim 4\text{--}8 \text{ kpc}$. This improved distance estimate will have implications for models of GRS 1716–249 that depend on its distance (e.g., Bassi et al. 2020; Chatterjee et al. 2021; Zhang et al. 2022) and affect the parameters of GRS 1716–249, like the inferred masses, spins, and inclination angles, which depends critically on the assumption of $d = 2.4 \text{ kpc}$ (Tao et al. 2019). For example, the same spectral modeling assuming a distance of $d = 8 \text{ kpc}$ results in $M_{\text{BH}} = 24.8^{+1.7}_{-10.2} M_{\odot}$ (compared to $M_{\text{BH}} = 7.6^{+0.8}_{-2.7} M_{\odot}$ obtained assuming $d = 2.4 \text{ kpc}$), which shows that the parameters of the system are clearly model dependent and sensitive to the distance (Lian Tao, private communication). So distances beyond 8 kpc would make it the most massive stellar-mass BH known in our Galaxy (Cyg X-1 currently holds the record with $21.2 \pm 2.2 M_{\odot}$, Miller-Jones et al. 2021), which is unlikely. This implies that a distance above 8 kpc is highly implausible and again argues for an upper limit that is substantially lower than 17 kpc .

A greater distance than the literature value also changes the position of the source in the radio/X-ray luminosity correlation plot (Bassi et al. 2019). Generally, BHXBs follow two different tracks in the radio/X-ray luminosity correlation plot (where $L_R \propto L_X^{\beta}$) – the “standard” track with a power-law index $\beta \sim 0.5\text{--}0.7$ (e.g., Corbel et al. 2003, 2013; Gallo et al. 2018), and the much steeper “outlier” track with $\beta \geq 1$ (e.g., Corbel et al. 2004; Coriat et al. 2011; Gallo et al. 2012), although the existence of two separate tracks has been questioned statistically (e.g., Gallo et al. 2014, 2018). Newer studies have also shown that the two tracks are not well defined and there is evidence for standard track sources to get steeper at high X-ray luminosity (Koljonen & Russell 2019), and outlier track sources to get shallower and ultimately rejoin the standard track at low X-ray luminosities (see, e.g., Coriat et al. 2011; Carotenuto et al. 2021). Although the underlying physics behind the two tracks is not completely clear, it has been suggested that the dichotomy could originate either from the

structure of the inner accretion flow or from different physical properties of the jets resulting in different levels of radio emission (Coriat et al. 2011). NSXBs, especially in the hard state, also showed a similar correlation with fainter radio emission compared to BHs and a steeper slope (with $\beta \sim 1.4$, e.g., Fender & Hendry 2000; Fender & Kuulkers 2001), although there is strong evidence of different classes of NSXBs showing different behavior in the radio/X-ray correlation plane (see, e.g., Tudor et al. 2017; van den Eijnden et al. 2021). We find that a greater distance shifts GRS 1716–249 from the lower-luminosity part of the outlier track (luminosities where mostly NSs are observed and the BHs seem to shift to the standard track) to the higher luminosities where the majority of the BHXB sample following the outlier track lies (see Figure 12). A greater distance also implies that the source was potentially formed in the bulge, and hence its proper motion is not necessarily representative of its natal kick, since the bulge itself has a large velocity dispersion and scale height (Atri et al. 2019).

5. Conclusion

The 2016–2017 outburst of the BHXB GRS 1716–249 (or GRO J1719–24) is well-studied at X-ray and radio wavelengths. In this work, we investigate the optical, near-IR, mid-IR, and UV wavelength monitoring data of GRS 1716–249 in outburst using LCO, REM, VLT (VISIR), and Swift’s UVOT, and compare them with the multiwavelength archival data from Gaia, Mount Abu 1.2 meter telescope, Swift XRT, NuSTAR, MAXI, ATCA, VLA, and LBA. We also report the long-term ($\sim 10 \text{ yr}$) optical light curve of the source using LCO and find that the quiescent i' -band magnitude is $21.39 \pm 0.15 \text{ mag}$.

We find that the optical and UV emission of the source in outburst is mainly originating from a multi-temperature accretion disk, with X-ray reprocessing dominating at high luminosities, and with some contribution at the fainter end from the viscously heated disk. Although the near-IR emission is dominated by the emission from the accretion disk, it has a weak contribution from the variable jet in a few epochs in the K band. The mid-IR and radio emission of the source are dominated by the synchrotron emission from a compact jet. In the hard state, the optical/UV emission of the source is correlated with both the soft and hard X-ray emission. The power-law coefficient of the correlation is consistent with the optical emission coming from an X-ray irradiated accretion disk with possibly some additional contribution from the viscous disk, as a hint of a shallower coefficient at low luminosities. This is also supported by the spectral energy distributions, variability studies and color–magnitude diagrams of the source during the outburst.

Finally, we discuss how the previous estimates of system parameters of the source (especially its mass and distance) are based on various assumptions, and cannot be completely trusted. From the global optical/X-ray correlation study in comparison with other black hole and neutron star X-ray binaries, and several other lines of reasoning, we show that GRS 1716–249 is much further away than what has previously been assumed, with a probable distance within the range $4\text{--}17 \text{ kpc}$, and a most likely range of $\sim 4\text{--}8 \text{ kpc}$.








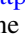








The authors thank the anonymous referee for useful comments and suggestions. The authors also thank Lian Tao for the revised black hole mass estimation using the updated



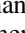




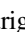

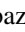



distance. D.M.R. and D.M.B. acknowledge the support of the NYU Abu Dhabi Research Enhancement Fund under grant RE124. J.J. acknowledges the support of the Leverhulme Trust, the Isaac Newton Trust, and St. Edmund's college, University of Cambridge. R.S. acknowledges grant No. 12073029 from the Natural National Science Foundation of China (NSFC). S. M. is thankful for support by Dutch Research Council (NWO) VICI award, grant Nr. 639.043.513. T.M.B. acknowledges financial contribution from the agreement ASI- INAF n.2017-14-H.0 and from PRIN-INAF 2019 N.15. T.D.R. acknowledges financial contribution from the agreement ASI-INAF n.2017-14-H.0. T.S. acknowledges financial support from the Spanish Ministry of Science, Innovation and Universities (MICIU) under grant PID2020-114822GB-I00. G.R.S. is supported by NSERC Discovery Grants RGPIN-2016-06569 and RGPIN-2021-0400. K.I.I.K. acknowledges funding from the European Research Council (ERC) under the European Union's Horizon 2020 research and innovation program (grant agreement No. 101002352) and from the Academy of Finland projects 320045 and 320085. This work uses data from the Faulkes Telescope Project, which is an education partner of Las Cumbres Observatory (LCO). The Faulkes Telescopes are maintained and operated by LCO. This work also uses observations made with the REM Telescope, INAF Chile. It is also based on observations collected at the European Southern Observatory under ESO programmes 098.D-0893 and 099.D-0884 (PI: D. Russell). Support for this work was provided by NASA through the NASA Hubble Fellowship grant HST-HF2-51494.001 awarded by the Space Telescope Science Institute, which is operated by the Association of Universities for Research in Astronomy, Inc., for NASA, under contract NAS5-26555. This work also makes use of data supplied by the UK *Swift* Science Data Centre at the University of Leicester, and the MAXI data provided by RIKEN, JAXA, and the MAXI team.

Appendix A Appendix Information

A detailed observation log of the optical detections containing information about the LCO epochs, filters, magnitudes and uncertainties is summarized in Table A1. The infrared detections including the REM epochs, filters, magnitudes and uncertainties are tabulated in Table A2).

ORCID iDs

Payaswini Saikia  <https://orcid.org/0000-0002-5319-6620>
David M. Russell  <https://orcid.org/0000-0002-3500-631X>
M. C. Baglio  <https://orcid.org/0000-0003-1285-4057>
D. M. Bramich  <https://orcid.org/0000-0002-1583-6519>
Piergiorgio Casella  <https://orcid.org/0000-0002-0752-3301>
Maria Diaz Trigo  <https://orcid.org/0000-0001-7796-4279>
Poshak Gandhi  <https://orcid.org/0000-0003-3105-2615>
Jiachen Jiang  <https://orcid.org/0000-0002-9639-4352>
Thomas Maccarone  <https://orcid.org/0000-0003-0976-4755>
Roberto Soria  <https://orcid.org/0000-0002-4622-796X>
Hind Al Noori  <https://orcid.org/0000-0002-4187-4981>
Aisha Al Yazeedi  <https://orcid.org/0000-0003-2577-6799>
Kevin Alabarta  <https://orcid.org/0000-0003-0168-9906>
Tomaso Belloni  <https://orcid.org/0000-0001-9621-3796>
Chiara Ceccobello  <https://orcid.org/0000-0002-4767-9925>
Stéphane Corbel  <https://orcid.org/0000-0001-5538-5831>

Rob Fender  <https://orcid.org/0000-0002-5654-2744>
Elena Gallo  <https://orcid.org/0000-0001-5802-6041>
Jeroen Homan  <https://orcid.org/0000-0001-8371-2713>
Karri Koljonen  <https://orcid.org/0000-0002-9677-1533>
Fraser Lewis  <https://orcid.org/0000-0003-3352-2334>
Sera B. Markoff  <https://orcid.org/0000-0001-9564-0876>
James C. A. Miller-Jones  <https://orcid.org/0000-0003-3124-2814>
Jerome Rodriguez  <https://orcid.org/0000-0002-4151-4468>
Thomas D. Russell  <https://orcid.org/0000-0002-7930-2276>
Tariq Shahbaz  <https://orcid.org/0000-0003-1331-5442>
Gregory R. Sivakoff  <https://orcid.org/0000-0001-6682-916X>
Vincenzo Testa  <https://orcid.org/0000-0003-1033-1340>
Alexandra J. Tetarenko  <https://orcid.org/0000-0003-3906-4354>

References

- Alabarta, K., Altamirano, D., Mendez, M., et al. 2020, *MNRAS*, **497**, 3896
Alabarta, K., Altamirano, D., Mendez, M., et al. 2021, *MNRAS*, **507**, 5507
Armas Padilla, M., Degenaar, N., Russell, D. M., & Wijnands, R. 2013, *MNRAS*, **428**, 3083
Armas Padilla, M., & Munoz-Darias, T. 2017, *ATel*, **10236**
Atri, P., Miller-Jones, J. C. A., Bahramian, A., et al. 2019, *MNRAS*, **489**, 3116
Baglio, M. C., Russell, D. M., Casella, P., et al. 2018, *ApJ*, **867**, 114
Baglio, M. C., Saikia, P., Russell, D. M., et al. 2022, *ApJ*, **930**, 20
Bahramian, A., Heinke, C. O., Degenaar, N., et al. 2015, *MNRAS*, **452**, 3475
Bahramian, A., Miller-Jones, J., Strader, J., et al. 2018, Radio/X-ray correlation database for X-ray binaries v0.1, Zenodo, doi:10.5281/zenodo.1252036
Bassi, T., Del Santo, M., Dai, A., et al. 2019, *MNRAS*, **482**, 1587
Bassi, T., Del Santo, M., & Motta, S. E. 2017, *ATel*, **10371**
Bassi, T., Malzac, J., Del Santo, M., et al. 2020, *MNRAS*, **494**, 571
Belloni, T. M. 2010, in *The Jet Paradigm*, ed. T. Belloni, Vol. 794 (Berlin: Springer), 53
Belloni, T. M., Colombo, A. P., Homan, J., et al. 2002, *A&A*, **390**, 199
Bernardini, F., Russell, D. M., Kolojnen, K. I. I., et al. 2016, *ApJ*, **826**, 149
Bharali, P., Chandra, S., Chauhan, J., et al. 2019, *MNRAS*, **487**, 3150
Blandford, R. D., & Konigl, A. 1979, *ApJ*, **232**, 34
Bramich, D. M., & Freudling, W. 2012, *MNRAS*, **424**, 1584
Brown, A. G. A., Vallenari, A., Prusti, T., et al. 2016, *A&A*, **595**, A2
Buxton, M. M., & Bailyn, C. D. 2004, *ApJ*, **615**, 880
Cadolle Bel, M., Rodriguez, J., D'Avanzo, P., et al. 2011, *A&A*, **534**, A119
Capitanio, F., Belloni, T., Del Santo, M., & Ubertini, P. 2009, *MNRAS*, **398**, 1194
Cardelli, J. A., Clayton, G. C., & Mathis, J. S. 1989, *ApJ*, **345**, 245
Carotenuto, F., Corbel, S., Tremou, E., et al. 2021, *MNRAS*, **504**, 444
Casares, J., & Jonker, P. G. 2014, *SSRv*, **183**, 223
Chatterjee, K., Debnath, D., Chatterjee, D., et al. 2021, *Ap&SS*, **366**, 63
Chaty, S., Mirabel, I. F., Goldoni, P., et al. 2002, *MNRAS*, **331**, 1065
Chaty, S., Munoz Arjonilla, A. J., & Dubus, G. 2015, *A&A*, **577**, A101
Chevalier, C., Illovaisky, S. A., van Paradijs, J., Pedersen, H., & van der Klis, M. 1989, *A&A*, **210**, 114
Corbel, S., Coriat, M., Brocksopp, C., et al. 2013, *MNRAS*, **428**, 2500
Corbel, S., & Fender, R. P. 2002, *ApJ*, **573**, L35
Corbel, S., Fender, R. P., Tomsick, J. A., Tzioumis, A. K., & Tingay, S. 2004, *ApJ*, **617**, 1272
Corbel, S., Fender, R. P., Tzioumis, A. K., et al. 2000, *A&A*, **359**, 251
Corbel, S., Nowak, M. A., Fender, R. P., Tzioumis, A. K., & Markoff, S. 2003, *A&A*, **400**, 1007
Coriat, M., Corbel, S., Buxton, M. M., et al. 2009, *MNRAS*, **400**, 123
Coriat, M., Corbel, S., Prat, L., et al. 2011, *MNRAS*, **414**, 677
Corral-Santana, J. M., Casares, J., Muñoz-Darias, T., et al. 2016, *A&A*, **587**, A61
Cuneo, V. A., Munoz-Darias, T., Sanchez-Sierras, J., et al. 2020, *MNRAS*, **498**, 25
Cunningham, C. 1976, *ApJ*, **208**, 534
Curran, P. A., & Chaty, S. 2013, *A&A*, **557**, A45
Curran, P. A., Chaty, S., & Zurita Heras, J. A. 2012, *A&A*, **547**, A41
Del Santo, M., Ducci, L., Miller-Jones, J., et al. 2017, *ATel*, **10069**, 1
della Valle, M., Mirabel, I. F., Cordier, B., et al. 1993, *IAU Circ.*, **5876**, 1

- della Valle, M., Mirabel, I. F., & Rodriguez, L. F. 1994, *A&A*, **290**, 803
- Done, C., Gierlinski, M., & Kubota, A. 2007, *A&AR*, **15**, 1
- Evans, P. A., Beardmore, A. P., Page, K. L., et al. 2007, *A&A*, **469**, 379
- Evans, P. A., Beardmore, A. P., Page, K. L., et al. 2009, *MNRAS*, **397**, 1177
- Falcke, H., Koering, E., & Markoff, S. 2004, *A&A*, **414**, 895
- Fender, R. P., Belloni, T. M., & Gallo, E. 2004, *MNRAS*, **355**, 1105
- Fender, R. P., & Hendry, M. A. 2000, *MNRAS*, **317**, 1
- Fender, R. P., & Kuulkers, E. 2001, *MNRAS*, **324**, 923
- Fender, R. P., Corbel, S., Tzioumis, T., et al. 1999, *ApJ*, **519**, L165
- Fitzpatrick, E. L. 1999, *PASP*, **111**, 63
- Foight, D. R., Guver, T., Ozel, F., & Slane, P. O. 2016, *ApJ*, **826**, 66
- Frank, J., King, A., & Raine, D. J. 2002, *Accretion Power in Astrophysics* (3rd ed.; Cambridge: Cambridge Univ. Press)
- Gallo, E., Degenaar, N., & van den Eijnden, J. 2018, *MNRAS*, **478**, L132
- Gallo, E., Miller, B. P., & Fender, R. 2012, *MNRAS*, **423**, 590
- Gallo, E., Miller-Jones, J. C. A., Russell, D. M., et al. 2014, *MNRAS*, **445**, 290
- Gandhi, P. 2009, *ApJ*, **697**, L167
- Gandhi, P., Blain, A. W., Russell, D. M., et al. 2011, *ApJ*, **740**, L13
- Gandhi, P., Dhillon, V. S., Durant, M., et al. 2010, *MNRAS*, **407**, 2166
- Gandhi, P., Littlefair, S. P., Hardy, L. K., et al. 2016, *MNRAS*, **459**, 554
- Gandhi, P., Rao, A., Johnson, M. A. C., Paice, J. A., & Maccarone, T. J. 2019, *MNRAS*, **485**, 2642
- Goodwin, A. J., Russell, D. M., Galloway, D. K., et al. 2020, *MNRAS*, **498**, 3429
- Guver, T., & Ozel, F. 2009, *MNRAS*, **400**, 2050
- Haswell, C., King, A. R., Murray, J. R., & Charles, P. A. 2001, *MNRAS*, **321**, 475
- Heinke, C. O., Bahramian, A., Degenaar, N., & Wijnands, R. 2015, *MNRAS*, **447**, 3034
- Hjellming, R. M., & Johnston, K. J. 1988, *ApJ*, **328**, 600
- Hjellming, R. M., Rupen, M. P., Shrader, C. R., et al. 1996, *ApJ*, **470**, L105
- Homan, J., & Belloni, T. 2005, *Ap&SS*, **300**, 107
- Homan, J., Buxton, M., Markoff, S., et al. 2005, *ApJ*, **624**, 295
- Homan, J., Wijnands, R., Kong, A., et al. 2006, *MNRAS*, **366**, 235
- Homan, J., Wijnands, R., van der Klis, M., et al. 2001, *ApJS*, **132**, 377
- Hynes, R. I. 2005, *ApJ*, **623**, 1026
- Hynes, R. I., Haswell, C. A., Cui, W., et al. 2003, *MNRAS*, **345**, 292
- Hynes, R. I., O'Brien, K., Horne, K., Chen, W., & Haswell, C. A. 1998, *MNRAS*, **299**, L37
- Hynes, R. I., O'Brien, K., Mullally, F., & Ashcraft, T. 2009, *MNRAS*, **399**, 281
- Hynes, R. I., Robinson, E. L., Pearson, K. J., et al. 2006, *ApJ*, **651**, 401
- Hynes, R. I., Robinson, E. L., Terndrup, D. M., et al. 2019, *MNRAS*, **487**, 60
- Ingram, A. R., & Motta, S. E. 2019, *NewAR*, **85**, 101524
- Jain, R. K., Bailyn, C. D., Orosz, J. A., McClintock, J. E., & Remillard, R. A. 2001, *ApJ*, **554**, L181
- Jiang, J., Furst, F., Walton, D. J., Parker, M. L., & Fabian, A. C. 2020, *MNRAS*, **492**, 1947
- Joshi, V., Vadwale, S., Ganesh, S., & Aarthy, E. 2017, *ATel*, **10196**
- Kalemci, E., Dinçer, T., Tomsick, J. A., et al. 2013, *ApJ*, **779**, 95
- Koljonen, K. I. I., Maccarone, T., McCollough, M. L., et al. 2018, *A&A*, **612**, A27
- Koljonen, K. I. I., & Russell, D. M. 2019, *ApJ*, **871**, 8
- Koljonen, K. I. I., Russell, D. M., Corral-Santana, J. M., et al. 2016, *MNRAS*, **460**, 942
- Koljonen, K. I. I., Russell, D. M., Fernández-Ontiveros, J. A., et al. 2015, *ApJ*, **814**, 139
- Krimm, H. A., Holland, S. T., Corbet, R. H. D., et al. 2013, *ApJSS*, **209**, 14
- Lagage, P. O., Pel, J., Authier, M., et al. 2004, *Msngr*, **117**, 12
- Lewis, F. 2018, *RTSRE*, **1**, 237
- Lewis, F., Russell, D. M., Fender, R. P., Roche, P., & Clark, J. S. 2008, in *AIP Conf. Proc.* 1010, *A Population Explosion: The Nature & Evolution of X-ray Binaries in Diverse Environments* (Melville, NY: AIP), 204
- Maccarone, T. J. 2003, *A&A*, **409**, 697
- Maitra, D., & Bailyn, C. D. 2008, *ApJ*, **688**, 537
- Maitra, D., Scarpaci, J. F., Grinberg, V., et al. 2017, *ApJ*, **851**, 148
- Mandel, I., & Muller, B. 2020, *MNRAS*, **499**, 3214
- Markoff, S., Falcke, H., & Fender, R. 2001, *A&A*, **372**, L25
- Masetti, N., Bianchini, A., Bonibaker, J., della Valle, M., & Vio, R. 1996, *A&A*, **314**, 123
- Masumitsu, T., Tanaka, K., Kawase, T., et al. 2016, *ATel*, **9895**, 1
- Mathis 1990, *ARA&A*, **28**, 37
- Matsuoka, M., Kawasaki, K., Ueno, S., et al. 2009, *PASJ*, **61**, 999
- McCully, C., Volgenau, N. H., Harbeck, D.-R., et al. 2018, *Proc. SPIE*, **10707**, 107070K
- Merloni, A., Heinz, S., & di Matteo, T. 2003, *MNRAS*, **345**, 1057
- Miller, J. M., Fabian, A., Kaastra, J., et al. 2017, *ATel*, **10296**, 1
- Miller-Jones, J. C. A., Sivakoff, G. R., Altamirano, D., et al. 2012, *MNRAS*, **421**, 468
- Miller-Jones, J. C. A., Bahramian, A., Orosz, J. A., et al. 2021, *Sci*, **371**, 1046
- Miyamoto, S., Kitamoto, S., Hayashida, K., & Egoshi, W. 1995, *ApJ*, **442**, L13
- Negoro, H., Masumitsu, T., Kawase, T., et al. 2016, *ATel*, **9876**, 1
- O'Brien, K., Horne, K., Hynes, R. I., et al. 2002, *MNRAS*, **334**, 426
- Oates, S. R., Motta, S., Beardmore, A. P., et al. 2019, *MNRAS*, **488**, 4843
- Paice, J. A., Gandhi, P., Charles, P. A., et al. 2019, *MNRAS*, **488**, 512
- Patruno, A., Maitra, D., Curran, P. A., et al. 2016, *ApJ*, **817**, 100
- Pirbhoy, S. F., Baglio, M. C., Russell, D. M., et al. 2020, *ATel*, **13451**
- Revnivtsev, M., Gilfanov, M., Churazov, E., et al. 1998, *A&A*, **331**, 557
- Revnivtsev, Sunyaev R. A. 2000, *AAP*, **358**, 617
- Ross, R. R., & Fabian, A. C. 2007, *MNRAS*, **381**, 1697
- Rout, S. K., Vadawale, S. V., Aarthy, E., et al. 2021, *JApA*, **42**, 39
- Russell, D. M., Bramich, D. M., Lewis, F., et al. 2019, *AN*, **340**, 278
- Russell, D. M., Casella, P., Kalemci, E., et al. 2020, *MNRAS*, **495**, 182
- Russell, D. M., Fender, R. P., Hynes, R. I., et al. 2006, *MNRAS*, **371**, 1334
- Russell, D. M., Fender, R. P., & Jonker, P. G. 2007, *MNRAS*, **379**, 1108
- Russell, D. M., Maitra, D., Dunn, R. J. H., & Fender, R. P. 2011, *MNRAS*, **416**, 2311
- Russell, D. M., Miller-Jones, J. C. A., Maccarone, T. J., et al. 2011, *ApJ*, **739**, L19
- Russell, D. M., Markoff, S., Casella, P., et al. 2013, *MNRAS*, **429**, 815
- Russell, T. D., Tetarenko, A. J., Miller-Jones, J. C. A., et al. 2019, *ApJ*, **883**, 198
- Rykoff, E. S., Miller, J. M., Steeghs, D., & Torres, M. A. P. 2007, *ApJ*, **666**, 1129
- Saikia, P., Koering, E., Coppejans, D. L., et al. 2018, *A&A*, **616**, A152
- Saikia, P., Koering, E., & Falcke, H. 2015, *MNRAS*, **450**, 2317
- Saikia, P., Russell, D. M., Pirbhoy, S. F., et al. 2022, *ApJ*, submitted
- Saikia, P., Russell, D. M., Bramich, D. M., et al. 2019, *ApJ*, **887**, 21
- Shahbaz, T., Linares, M., Nevado, S. P., et al. 2015, *MNRAS*, **453**, 3461
- Shahbaz, T., Russell, D. M., Zurita, C., et al. 2013, *MNRAS*, **434**, 2696
- Shakura, N., & Sunyaev, R. A. 1973, *A&A*, **24**, 337
- Skrutskie, M. F. 2006, *AJ*, **131**, 1163
- Stetson, P. B. 1990, *PASP*, **102**, 932
- Sunyaev, R. A., & Titarchuk, L. G. 1980, *A&A*, **86**, 121
- Tananbaum, H., Gursky, H., Kellogg, E., Giacconi, R., & Jones, C. 1972, *ApJ*, **177**, L5
- Tao, L., Tomsick, J. A., Qu, J., et al. 2019, *ApJ*, **887**, 184
- Tetarenko, A. J., Casella, P., Miller-Jones, J. C. A., et al. 2021, *MNRAS*, **504**, 3862
- Tetarenko, B. E., Dubus, G., Marcel, G., Done, C., & Clavel, M. 2020, *MNRAS*, **495**, 3666
- Tetarenko, B. E., Sivakoff, G. R., Heinke, C. O., & Gladstone, J. C. 2016, *ApJS*, **222**, 15
- Thorne, K. S., & Price, R. H. 1975, *ApJ*, **195**, L101
- Tonry, J. L., Denneau, L., Flewelling, H., et al. 2018, *ApJ*, **867**, 105
- Torres, M. A. P., Jonker, P. G., Casares, J., Miller-Jones, J. C. A., & Steeghs, D. 2021, *MNRAS*, **501**, 2174
- Tudor, V., Miller-Jones, J. C. A., Patruno, A., et al. 2017, *MNRAS*, **470**, 324
- Vahdat Motlagh, A., Kalemci, E., & Maccarone, T. J. 2019, *MNRAS*, **485**, 2744
- van den Eijnden, J., Degenaar, N., Russell, T. D., et al. 2021, *MNRAS*, **507**, 3899
- c van der Horst, A. J., Curran, P. A., Miller-Jones, J. C. A., et al. 2013, *MNRAS*, **436**, 2625
- van Paradijs, J. 1981, *A&A*, **103**, 140
- van Paradijs, J., & McClintock, J. E. 1994, *A&A*, **290**, 133
- Vaughan, S., Edelson, R., Warwick, R. S., et al. 2003, *MNRAS*, **345**, 1271
- Veledina, A., Poutanen, J., & Vurm, I. 2013, *MNRAS*, **430**, 3196
- Vincentelli, F. M., Casella, P., Maccarone, T. J., et al. 2018, *MNRAS*, **477**, 4524
- Vrtilek, S. D., Raymond, J. C., Garcia, M. R., et al. 1990, *A&A*, **235**, 162
- Watson, D., & 2011, A. 2011, *A&A*, **533**, A16
- Willingale, R., Starling, L. C., Beardmore, A. P., Tanvir, N. R., & O'Brien, P. T. 2013, *MNRAS*, **431**, 394
- Zhang, G.-B., Bernardini, F., Russell, D. M., et al. 2019, *ApJ*, **876**, 5
- Zhang, Z., Liu, H., Abdikamalov, A. B., et al. 2022, *ApJ*, **924**, 72